Schottky contacts and electrical characterization of *n*-type hydrothermally grown ZnO

by

Ramón Schifano

Submitted

in partial fulfillment of the requirements

for the degree of

Philosophiae Doctor

Department of Physics/Center for Materials Science and Nanotechnology

Faculty of Mathematics and Natural Sciences

University of Oslo

© Ramón Schifano, 2009

Series of dissertations submitted to the
Faculty of Mathematics and Natural Sciences, University of Oslo
Nr. 869

ISSN 1501-7710

All rights reserved. No part of this publication may be
reproduced or transmitted, in any form or by any means, without permission.

Cover: Inger Sandved Anfinsen.
Printed in Norway: AiT e-dit AS, Oslo, 2009.

Produced in co-operation with Unipub AS.
The thesis is produced by Unipub AS merely in connection with the
thesis defence. Kindly direct all inquiries regarding the thesis to the copyright
holder or the unit which grants the doctorate.

Unipub AS is owned by
The University Foundation for Student Life (SiO)

Abstract

Wide band gap semiconductors, like SIC, GaN, ZnO and diamond represent new semiconductor materials that offer advantages in terms of power capability (DC and microwave), ionizing radiation insensitivity, high temperature and high frequency operation and optical properties with respect to the nowadays most commonly used semiconductors Si and GaAs. At the present devices based on GaN and SiC used mainly for microwave applications and for power supplies and motor controls, respectively, are already commercial available. On the other hand, ZnO use is established in applications like transparent electrodes in flat panels and solar cells. In addition, recently ZnO is strongly emerging as an alternative for optoelectronic applications and has boosted the recent increased interest. While, the control of material properties has been improved, and first electronic and optoelectronic devices have been reported still some basic properties are still unclear and some key issues have not been accomplished.

The electrical characterization represents an indispensable tool to establish semiconductor defect properties and in the case of ZnO is still lagging behind due, mostly, to the difficulties in achieving metal rectifying contacts that can be used to probe the material by junction spectroscopic techniques. In this thesis, a method for realizing rectifying metal/ZnO contacts based on a hydrogen peroxide pretreatment is described and the results found are among the most promising ones between the procedures investigated for obtaining or improving the rectifying contact performances reported in the literature so far. In addition, some insight into the physical mechanism beyond the superior rectification performances has been

obtained by combining electrical characterization and chemical analysis of the metal/semiconductor interface and bare surface properties with and without being hydrogen peroxide treated. Furthermore, the method investigated to realize highly rectifying metal semiconductor contacts has been employed to probe the ZnO band gap down to an energy ~ 0.3 eV below the conduction band edge (E_C) and study the role of Li, K, Na, Al, Ga and In that are common impurities in ZnO. Al is shown to provide a level ~ 60 meV below E_C, while it is found that group I elements are only partially responsible for the ZnO compensation. Finally, the negative-U nature of a level ~ 100 meV below E_C has been suggested.

Acknowledgements

"'Love is showing
to human beings
how they should be"
A. P. Cechov

First of all, I'm expressing my gratitude to my main supervisor Prof. Bengt Gunnar Svensson for giving me all the freedom and the support that I needed. During these years many times it happened that his confidence in me was higher than mine and without his experience, supervision and Swedish attitude this thesis would not have been accomplished. Then I'd like to thanks Dr. Ulrike Grossner and Dr. Eduard Monakhov for introducing me to the equipments in the laboratories and the measurements techniques. In addition, I'm especially indebted with them since they had the unpleasant task of reviewing the first version of the papers before submitting them to Bengt and fight against my tendency of writing very long sentences. I will work on it, I promise!
Also, the assistance of the group's engineers Viktor Bobal and Thomas Marthin-

sen in breathing new life in dead equipments and, in particular, the long time that we spent all together in understanding and fixing the Leybold e-beam was fundamental for achieving the results exposed in this thesis! Thanks to Spyros Diplas for the time spent in measuring and analyzing the XPS data and Anette, his wife, for her patience. Then, I'd like to thank my ZnO colleagues in MinaLab Dr. Lasse Vines and Klaus Johansen and just colleagues Dr. Jahn Bleka, Dr. Mayandi Jeyanthinath and Lars Løvlie for the many serious lab and semiconductor physics related talks and the much more less serious, sometimes C_2H_5OH spiced up, moments spent together. Also the daily reminders about itchy topics of my office mate pani Agnieszka compensated by the good karma of her husband, Paweł, and the original Indian one of Vishnu Venkatachalapathy definitively helped to see metal/semiconductor junctions from a different prospective.
A grazie for sharing with me the hard, normal and great moments of my norvegian life, dinners, pizzas, tramisú, dances and chats to all my friends here in Oslo, in Italy, my parents, the Sicilian grandma, the two Swiss super-couples and the highlanders Samuele i Kasia, there is a contribution of all of you here, even if, maybe, you are not aware about it.
Finally, I'd like to thank Prof. Danie Auret, Sergio and Janse van Rensburg for being great hosts both inside and outside the laboratory during my visit at the university of Pretoria.

Contents

1 Motivation and general background **1**

2 ZnO properties **4**

2.1 Basic characteristics of ZnO 4

2.2 Point defects and Impurities in ZnO 7

3 Schottky contacts **12**

3.1 Theory 12

3.1.1 Intimate contacts 15

3.1.2 Bardeen model 17

3.2 The state of the art 19

4 Experimental methods **24**

4.1 Atomic force microscopy 24

4.2 Current versus Voltage characterization 29

4.3 Capacitance versus Voltage characterization 32

4.4 Thermal admittance spectroscopy 38

4.4.1 Above the freeze out temperature of the charge carriers . . 39
4.4.2 The freeze out region of charge carriers 42
4.5 Temperature dependent Hall effect 44
4.5.1 Basic relationships 45
4.5.2 The procedure used in analyzing the Hall data 47

5 Summary of the results, conclusions and suggestions for further studies 51
5.1 Paper I 52
5.2 Paper II 53
5.3 Paper III 54
5.4 Paper IV 55
5.5 Paper V 55
5.6 Concluding remarks and suggestions for further studies 56

List of included papers

1. **Electrical characteristics of palladium Schottky contacts to hydrogen peroxide treated hydrothermally grown ZnO**
   R. Schifano, E. V. Monakhov, U. Grossner, and B. G. Svensson, *Appl. Phys. Lett.*, **91**, 193507, (2007)

2. **Surface passivation and interface reactions induced by hydrogen peroxide treatment of *n*-type ZnO** $(000\overline{1})$
   R. Schifano, E. V. Monakhov, B. G. Svensson and S. Diplas, *Appl. Phys. Lett.*, **94**, 132101 (2009)

3. **Defects in virgin hydrothermally grown *n*-type ZnO studied by temperature dependent Hall effect measurements**
   R. Schifano, E. V. Monakhov, B. G. Svensson, W. Mtangi and F. D. Auret *submitted to J. Appl. Phys.* (2009)

4. **Shallow levels in virgin hydrothermally grown *n*-type ZnO studied by thermal admittance spectroscopy**
   R. Schifano, E. V. Monakhov, B. G. Svensson, W. Mtangi, P. J. Janse van

Rensburg and F. D. Auret *accepted to be published in Physica B: Condensed Matter* (2009)

5. **Schottky contacts to hydrogen doped ZnO**
   R. Schifano, E. V. Monakhov, J. S. Christensen, A. Yu. Kuznetsov, and B. G. Svensson, *phys. stat. sol. (c)*, **205**, 1998, (2008)

Related publications not included in the thesis

1. **Investigation of contact material for cross section scanning spreading resistance microscopy on Zinc Oxide**
   K.M. Johansen, L. Vines, R. Schifano, E.V. Monakhov and B. G. Svensson, *phys. stat. sol. (c)*, **5**, 3361, (2008)

2. **Hydrothermally Grown Single-Crystalline Zinc Oxide; Characterization and Modification**
   B.G. Svensson, T. Moe Børseth, K.M. Johansen, T. Maqsood, R. Schifano, U. Grossner, J.S. Christensen, L. Vines, P. Klason, Q.X. Zhao, M. Willander, F. Tuomisto, W. Skorupa, E.V. Monakhov and A.Yu. Kuznetsov, *Materials Research Society Symposium Proceedings*, **1035**, L04-01 (2008)

Chapter 1

Motivation and general background

The present demand of short wavelength photonic devices and fast, high power and high temperature devices, to be used in a low energy consumption power electronics puts high requirements on the characteristic of the semiconducting material and the processing for device fabrication. This request of devices with superior and different performances compared to those based on more conventional semiconductors, silicon (Si) and gallium arsenide (GaAs), can be accomplished by using wide energy band gap semiconductors. Among the wide band gap semiconductors, especially diamond (C), silicon carbide (SiC), and gallium nitride (GaN) have been studied more in detail so far, but since a few years also wide band gap oxides, in particular zinc oxide (ZnO), have received substantial interest [1]. In the case of ZnO beside showing a wide and direct bandgap of 3.437 eV at 1.6 K [2], ZnO has some other appealing properties. It presents a free exciton binding

energy of about 60 meV [3], it is optical transparent even at high doping concentrations [4] and it is highly resistant to radiation damage [5]. In addition, a high electron saturation velocity is expected from theoretical predictions [6]. These properties could lead to the realization of light emitting diodes, transparent thin film transistor, high temperature, high power, high frequency electronic devices, to be used even in space applications and they are fundamental in already established ZnO applications like transparent electrodes in flat panel displays or solar cells. Moreover, the combination of a wide band gap with a high excitonic binding energy and the possibility of growing quantum wells by alloying it with Cd or Mg [7] paves the way to the fabrication of UV lasers based on excitonic recombination which is attractive for implementation of highly efficient opto-electronic devices. Furthermore, processing of ZnO for such devices appears viable: wet chemical etching [8] and low temperature epitaxial growth [9] are possible and there is a well developed technique for growing bulk material, i.e. it has a native substrate [10, 11, 12]. Among the most commonly used growth techniques for growing large area single crystal ZnO that is, by melt, chemical vapor deposition and hydrothermal technique, the latter is particularly interesting due to the fairly good quality of the substrates [13]and the possibility of scaling the growth method [14].

However, despite the revival of ZnO for a wide range of potential applications, some basic properties of ZnO remain still unclear and some central issues have not been resolved yet. Especially a reliable and reproducible method for achieving controllable p-type doping in ZnO has not yet been well accomplished [5]. In addition, rectifying contacts (Schottky contacts) are not straightforward to realize and high barrier reliable Schottky contacts with low reverse leakage current are

still lacking [15]. The accomplishment of p-doping and of good contacts, both rectifying and Ohmic ones, are crucial for the realization of the possible applications discussed above. Not less important, good quality contacts are indispensable for electrical characterization of the material: for instance, electrical characterization provides insight on dopants, charge carrier concentration, mobility and the nature of electrically active defects, and can contribute significantly to improve the material.

The results presented in this thesis deal mainly with the realization of high quality Schottky contacts (*SC*s) on *n*-type ZnO. It is shown that after a pretreatment involving a dip in H_2O_2 *SC*s with a sufficiently high rectification ratio to allow the electrical characterization of the material by junction spectroscopic techniques are demonstrated and the results of the subsequent characterization of hydrothermally grown *n*-type ZnO are shown.

Chapter 2

ZnO properties

In this chapter some of the established information of the structural and electrical properties of ZnO needed for a better understanding of the experimental methods and the results described in the papers attached are summarized.

2.1 Basic characteristics of ZnO

ZnO crystallizes in three lattice types: rock salt, zincblende and wurtzite. Bulk ZnO at ambient pressure is only stable in the wurtzite structure shown in Fig. 2.1. This structure is characterized by an hexagonal unit cell with two lattice parameters [16] $a = 3.25 \pm 0.03$ $\AA$ and $c = 5.21 \pm 0.03$ $\AA$ and may be regarded as two inter-penetrating close packed hexagonal sub-lattices where each sub-lattice consists of one type of atom (zinc and oxygen, respectively). The two sub-lattices

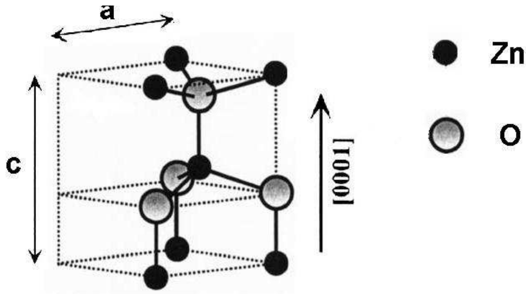

Figure 2.1: The ZnO stable crystal structure, the two lattice parameters characterizing the hexagonal wurtzite structure and the [0001] direction pointing from the O-face to the Zn-face are indicated as well.

are shifted relative to each other along the common c-axis ([0 0 0 1] direction). Hence, it is worth to notice that the wurtzite crystal structure does not posses an inversion symmetry and hence a crystal polarity appears. Many material properties like for example growth rate of epitaxial layers, etching and defect formation depend on the face that is exposed.

In particular, due to the above mentioned polarity the O-face and the Zn-face are expected to be unstable [17] and reconstruction [18] and/or interaction with electro-positive and electro-negative elements can play an important role for stabilizing the surfaces [19]. In addition, it has been suggested [20] that a higher Schottky barrier height (ϕ_B) is expected on the Zn-face as an effect of an upward band bending on this face caused by the intrinsic polarization. However, the samples studied in this thesis were cut with the *c*-axis perpendicular to the surface and excellent Pd *SC*s were obtained on the O-face. In fact, after a pretreatment involving a dip in H_2O_2 *SC*s with a sufficiently high rectification ratio to allow the electrical characterization of the material by junction spectroscopic techniques are

demonstrated.

Other material parameters relevant to the thesis have been taken from the literature and are listed in Table 2.1. In the first row, the band gap temperature dependence ($E_G(T)$) is reported. This relation describes the decrease in the band gap width with increasing temperature due to the material thermal expansion and the one electron-phonon interaction [25, 26] up to $\sim$ 300 K. $\varepsilon_{r\,||}$ and $\varepsilon_{\infty\,||}$ are the static and high frequency permittivity parallel to the c axis, respectively, while $\varepsilon_{r\,\perp}$ and $\varepsilon_{\infty\,\perp}$ are the corresponding ones orthogonal to the c axis. m^* is the polaron mass in a.m.u., ε_{ac} the deformation potential, c_l the longitudinal elastic constant, T_{po} the equivalent temperature of the longitudinal optical phonons (LO) corresponding to a phonon energy of $\sim$ 71 meV, N_{dis} and Q the dislocation density typical for hydrothermally grown ZnO and the dislocation charge per unit length, respectively. The way these parameters contribute to the carrier concentration and mobility

Table 2.1: ZnO constants used for the electrical characterization analysis. Values (a) are from Ref. [1], (b) from Ref. [16], (c) from Ref. [21], (d) from Ref. [22], (e) from Ref. [23], (f) from Ref. [14] and (g) from Ref. [24]

$$E_G(T)^{\ a} = 3.4371 - (5.05 \times 10^{-4} \times T^2)/(900 - T)$$

$\varepsilon_{r\,\parallel}$ [b]	8.91	$\varepsilon_{\infty\,\parallel}$ [b]	3.78
$\varepsilon_{r\,\perp}$ [b]	7.77	$\varepsilon_{\infty\,\perp}$ [b]	3.70
m^* [c,d]	0.336	ε_{ac} [e] (eV)	3.8
$K_\perp$ [e]	0.21	c_l [e] (N m^{-2})	2.05 10^{11}
T_{po} [b] (K)	824		
N_{dis} [f] (cm^{-2})	10^4	Q [g] (C m^{-1})	2.7 10^{-10}

is described in detail in Chapter IV and in paper III, while here some common features are underlined. As revealed by Table 2.1 both the static and the high frequency permittivity display a directional dependence, due to the above mentioned crystal polarity and, in general, the material properties are expected to be anisotropic. In addition, as suggested by photoluminescence measurements [16], a strong coupling of the carriers with the *LO* occurs. This affects not only the mobility through its scattering contribution, but also alter considerably the electron effective mass, named in this case the polaron mass, that turns out to be larger than the bare conduction band edge effective mass [21, 23, 27].

2.2 Point defects and Impurities in ZnO

Typical defects occurring in ZnO are listed in Fig. 2.2. Interstitials (i) of the same type of atoms as the host, like Zn_i and O_i are named self-interstitials, otherwise an impurity can be involved and the symbol X_i is used in this case. An impurity X can, also, occupy a substitutional lattice site and replace a Zn or O atom, X_{Zn} and X_O, respectively. The Zn and O lattice sites can, also, be vacant and form a vacancy, V_{Zn} and V_O, respectively. Finally, the above mentioned defects can combine with themselves to form higher order complexes.

The properties of the defects and impurities in ZnO are still not understood and their characterization, as already mentioned, is lacking behind. This is mostly due to the difficulties in achieving stable *SC*s that are fundamental for studying defects in semiconductors by junction spectroscopy techniques like admittance spectroscopy (*AS*) and deep level transient spectroscopy (*DLTS*). Below some of the main established results related to defects and impurities, relevant to this

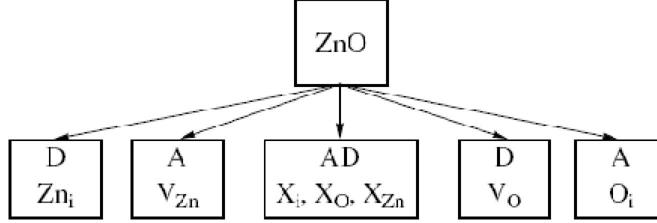

Figure 2.2: Summary of the point defects that may occur in ZnO, where A and D stand for acceptor and donor respectively. In the second row the intrinsic defects Zn_i, O_i, V_{Zn} and V_O, interstitial Zn, O and Zn and O vacancies, respectively and the interstitial and the substitutional defects involving an impurity *X* are listed.

thesis, are summarized.

Group III elements on Zn site, Al_{Zn}, Ga_{Zn} and In_{Zn} act as donors to ZnO resulting in *n*-type material with high conductivity and transparency in the visible wavelength range [28, 29, 30]. Their fingerprints in the band edge photoluminescence spectra have recently been attributed [2], while there is still some dispute on the assignment of the corresponding energy level position obtained from TDH measurements [1]. A level $\sim$ 80 meV below the conduction band edge[1] (E_C) is

[1]It is worth to remind that, in general, the activation energy (E_D) of a donor type element (D) depends on its concentration (N_D) due to the Coulomb screening effect [31]:

$$E_D(N_D = 0) = E_D + \beta N_D^{1/3} \tag{2.1}$$

where $\beta \sim 2-3 \times 10^{-5}$ meV cm for ZnO can be assumed [31]. The values of E_D listed in this section take into account this correction in order to provide values that are independent on N_D.

believed to be related to either Al or Ga, but in both cases their photoluminescence counterparts suggest a ~ 20 meV shallower position. Hydrogen is another well known impurity yielding *n*-type conductivity with a donor level ~ 50 meV below (E_C). Moreover, it has been demonstrated that irrespective of H is incorporated on interstitial site or in a V_O it always acts as s donor despite of the Fermi level position in the band-gap. Hence, considering that H is always present during the growth process, the unintentional *n*-type conductivity traditionally attributed to oxygen vacancies can have a substantial contribution from H related donors [32]. A third and more shallow level with an activation energy in the $\sim 30-40$ meV range is also commonly observed [1] in ZnO and a study based on electron irradiated material suggests an assignment to complexes involving Zn_i [33].
More deeper into the band gap, in the $\sim 70-150$ meV range below E_C, at least two other levels are reported to occur [34, 35, 36]. There is some evidence that one of them is donor related [34, 36], while the nature of the other one is almost completely unknown. Furthermore, discrepancies between their energy positions determined by temperature dependent Hall (TDH) measurements and $DLTS$ are found [34] and attributed to a temperature activated capture cross section. The level of unknown origin exhibits a metastable behavior: it is possible to introduce it by annealing under reverse bias at temperature above 130 K, while it can be removed by an annealing at zero bias and above 110 K.
Finally, two more levels are generally found in bulk ZnO [34, 35] ~ 0.3 and $\sim 0.5-0.6$ eV below E_C , frequently labelled E_3 and E_4, respectively. The latter one which displays a large capture cross section $\sim 10^{-12}$ cm^2, is supposed to be related to some unspecified extended defect of intrinsic nature. The former one, E_3, has been commonly attributed to V_O [37], but, recently also Fe or Ni impu-

rities [38] have been addressed as possible candidates. On the other hand E_3 is observed both in polycrystalline and single crystalline material irrespective of the growth technique used. Hence, an attribution to Fe or Ni impurities seems unrealistic, while an assignment to an intrinsic defect is favored. Results obtained in a recent study by Brauer et al. [39] based on a combined characterization by TDH, $DLTS$ and positron annihilation spectroscopy (PAS), seem indeed to confirm the intrinsic nature of E_3 and a tentative assignment of E_3 to the second ionization level of Zn_i is discussed, while the donor level in the $70-150$ eV, mentioned above is ascribed to V_O.
Theoretically, as depicted in Fig. 2.2 both O_i and V_{Zn} are expected to be acceptor like defects in ZnO [40]. Further known extrinsic acceptors in ZnO include group I elements on Zn site, Li_{Zn}, Na_{Zn} and K_{Zn}, and group V elements on O site like N_O, P_O, As_O and Sb_O [16]. As previously mentioned and despite of the wide range of possible candidates the realization of p-type doping is still challenging. In case a group I element, X, is used to realize p-doping self compensation, i.e. compensation between the acceptor X_{Zn} and the donor X_i, limits the effective hole concentration. For a group V element, Y, formation of donors associated with Y_{Zn} rather then acceptors states originating from Y_O represents the main reason for the difficulty in achieving p-doping according to theory [41]. Experimentally, successful realization of p-type ZnO has been reported using N [42], which is reasonable since nitrogen has a similar ionic radius as oxygen thus making it easily substitutable. P-type doping has also been achieved using P, Sb and As [43, 44, 45] and these elements might be, beside N, the most promising ones for realizing p-type conductivity. However, despite these promising reports, the major challenge still remains namely, the development of a reliable method to produce

highly conductive p-type layers and also to accomplish selective area doping.

Chapter 3

Schottky contacts

3.1 Theory

For understanding how a rectifying behavior can be obtained by depositing a metal layer to a semiconductor the energy band diagram of the metal and the semiconductor far from each other has to be considered first (Fig. 3.1(a)). The metal is characterized by its work function (ϕ_m) that is the energy needed to take an electron at the Fermi level (E_F^m) and place it outside the metal at rest (E_{vac}). On the other hand, in the case of a semiconductor, the important surface parameter for describing the metal-semiconductor interface is the electron affinity (χ_s) that is the energy difference between an electron at rest outside the semiconductor and one just inside the semiconductor at the bottom of the conduction band edge (E_c). Considering the case of a *n*-type semiconductor as shown in Fig. 3.1(a), when the

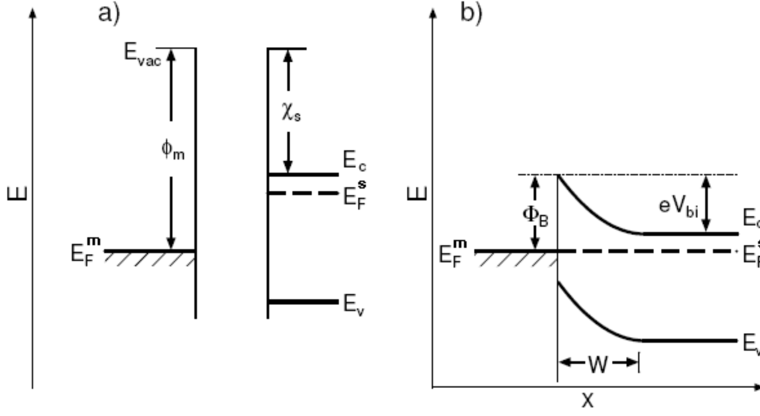

Figure 3.1: The energy band diagram of a metal and a *n*-type semiconductor isolated (a) and in perfect contact (b) from Ref. [47].

two materials are brought in contact electrons move from the semiconductors towards the lower energy states into the metal. As a result, a band bending occurs that lowers the semiconductor bulk mean electron energy, i.e. the metal and semiconductor Fermi levels to coincide over all the structure. As seen in Fig. 3.1(b), this results in the formation of a depleted region of width W and a barrier (Φ_b) of height [46]:

$$\Phi_b = \phi_m - \chi_s. \tag{3.1}$$

It is worth to point out that the situation depicted in Fig. 3.1(b) corresponds to a dynamic equilibrium, where the two currents, the one produced by electrons moving from the semiconductor towards the metal ($I_{s \to m}$) and the one caused by electrons moving from the metal to the semiconductor ($I_{m \to s}$), cancel. By biasing the contact the quasi Fermi level in the semiconductor can be moved with

respect to the one in the metal changing the effective barrier height (eV_{bi}) that an electron moving from the semiconductor towards the metal is experiencing without affecting the barrier (Φ_b) for an electron moving in the opposite direction. Then, the contact rectifying behavior is the consequence of the difference in the effective barrier heights controlled by the external bias for the current flows $I_{s\rightarrow m}$ and $I_{m\rightarrow s}$. Such a semiconductor-metal junction is defined as a Schottky contact (SC).

Some important assumptions have been made in establishing the barrier height according to the model above described, named the Schottky-Mott limit [46]:

1. no change in either ϕ_m or χ_s when the semiconductor and the metal are brought in contact

2. no electron states exist neither on the semiconductor surface nor at the metal-semiconductor interface

3. no interfacial layer exist, i.e. a perfect contact is formed between the metal and the semiconductor

In general, real *SC*s do not obey Eq. 3.1. For instance, in the case of *n*-Si and *n*-GaAs, where the contact properties have been extensively studied, metals with higher ϕ_m do give higher Φ_b, but the dependence of Φ_b on ϕ_m is substantially less than unity [48]. On the other hand, for ionic semiconductors like ZnO, a stronger dependence of Φ_b on the contact metal may be expected [49] in comparison to more covalent semiconductors like Si and GaAs; since the strong ionicity reduces the long range order effects making the above mentioned assumptions more valid. Hence, other models have been proposed to describe in detail more

metal-semiconductor junctions, and this holds in particular for the two following extreme limits: the intimate contact between the metal and the semiconductor (metal induced gap states) and the presence of a interfacial insulating layer (Bardeen model).

3.1.1 Intimate contacts

Intimate contacts can be obtained by depositing the metal on a surface that has been (i) heated, sputtered and annealed, (ii) cleaved or (iii) realized by deposition of the semiconducting material itself in situ, i.e. in the same chamber as where the subsequent metal deposition will occur, and obviously ultra high vacuum conditions are needed in this case. The expected abruptness of the metal-semiconductor interface facilitates a treatment of the whole system as a single entity and the structure represents a close to the ideal case to investigate the above mentioned dependence of Φ_b on the material ionicity, both from a theoretical and an experimental point of view. Calculations have been performed by Luie et al. [50] considering, for example, the metal as a jellium model[2] and taking into account just the crystal structure of the semiconductor. Essentially, the calculations show that, when the metal is present, the semiconductor band gap is closing nearby the interface within few atomic layers due to the conduction electron wave functions that tunnel from the metal into the semiconductor band gap. Hence, this implies the formation of interface states (metal induced gap states, *MIGS*) that can pin E_F and affect the dependence of Φ_b on the metal work function. As shown in Fig. 3.2, in high ionic semiconductors, like ZnS and ZnSe, the metal electrons penetrate less into the semiconductor compared to more covalent materials, like Si and GaAs, consistent with the experimentally found dependence of Φ_b on the material ionicity [46, 51].

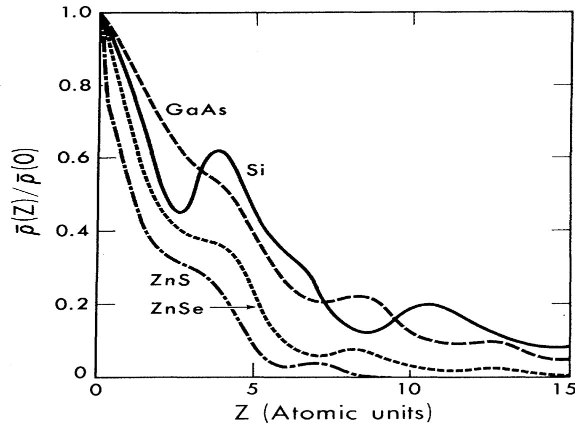

Figure 3.2: Relative charge distribution of the penetrating *MIGS* as a function of the distance from the metal-semiconductor interface (z=0) with Aluminium as the contact metal. The abscissa unit is the Bohr radius ($0.53\AA$) (from Ref. [50]).

Moreover, it is worth to notice that in reality the interface electronic structure, and consequently Φ_b, can be substantially influenced also by other factors [46]:

1. the metal-semiconductor interface might not be atomically abrupt, even if the deposition is made at room temperature, due to diffusion of metal atoms into the semiconductor and vice-versa.

2. the presence of interface reactions resulting in a compound layer.

[2]In the jellium model the metal positive ion cores are approximated by a positive uniform background smeared all over the material according to the metal density.

3. the surface structure of both the metal and the semiconductor may change during the deposition. In addition, because of differences between metal and semiconductor lattice parameters, misfit dislocations, strained layers and polycrystalline layers can form.

None of these three factors is taken into account by the simplistic model for intimate contacts summarized above.

3.1.2 Bardeen model

The generalized Bardeen model represents the other limiting case. Here, an insulating layer of thickness δ and interface states with a density per unit surface and energy of D_S (assumed constant through the whole band-gap) are considered to be present between the metal and the semiconductor, as shown in Fig. 3.3(a) and (b). The insulating layer is supposed to be thin enough to not affect the electron transfer from the metal to the semiconductor and vice-versa, and the interface state occupancy is determined by the E_F^m through tunneling to the conduction band states in the metal.

In this case, with ϕ_0 as the neutral level of the interface states[2] and assuming no changes in the metal ϕ_m or semiconductor χ_s due to the presence of the insulating film, the flat band barrier height (Φ_b^0), i.e. the barrier height when the applied voltage is such that there is no band bending in the semiconductor (Fig. 3.3(b)), can be derived as [46]:

$$\Phi_b^0 = \gamma\,(\phi_m - \chi_S) + (1-\gamma\,)\,(E_G - \phi_0) \tag{3.2}$$

with

[2] When (E_F^m) is above ϕ_0 then the net charge accommodated by the interface states is negative.

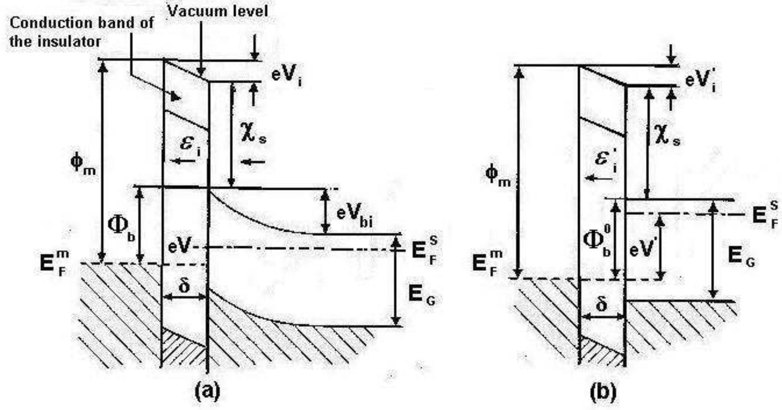

Figure 3.3: A metal semiconductor contact with an insulating interfacial layer of thickness δ and an arbitrary voltage applied (a) and in the flat band case (b) (that is when there is no electric field in the semiconductor). The Fermi level in the semiconductor (E_F^s) and in the metal (E_F^m), the voltage drop (V_i) and the electric field (ε_i) present in the insulating layer and the overall potential difference between metal and semiconductor (V) are indicated as well. Primed quantities are used in the case of the flat band condition, from Ref. [46].

$$\gamma = \frac{\varepsilon_0 \varepsilon_r}{\varepsilon_0 \varepsilon_r + e\delta D_S} \tag{3.3}$$

As expected, Eq. 3.2 reduces to the Schottky-Mott limit $\Phi_b = \phi_m - \chi_s$ when $D_S \rightarrow 0$ and to $E_G - \phi_0$ for $D_S \rightarrow \infty$. In the latter case, the high density of surface states pins E_F at ϕ_0 and the barrier height depends neither on the metal ϕ_m nor on the semiconductor χ_S anymore. Thus, the Bardeen model can explain qualitatively the weak dependence of Φ_b^0 on the metal ϕ_m relative to the one expected

according to the Schottky-Mott model. However, in practice the dependence of Φ_b^0 on ϕ_m predicted by Eq. 3.2 is usually not fulfilled, since D_S and its distribution through the band-gap depend on the metal-semiconductor combination and on the way the contact is made [52].

Finally, it should be emphasized that in the Bardeen model, due to the presence of the insulating layer, part of the voltage drop will occur between the semiconductor and the metal (indicated as V_i and V_i' in Fig. 3.3(a) and (b)) yielding a field dependence of the barrier height. The dependence of the barrier height on the applied voltage is important in connection to the *SC*s current vs voltage characteristics discussed in the next Chapter.

3.2 The state of the art

High quality *SC*s to ZnO are crucial both for device applications and for electrical characterization of the material. However, despite the first *SC* to ZnO was reported by Mead [51] already in 1965, it is still challenging to realize stable and high quality *SC*s. For instance, the presence of a conductive surface layer due to group III ions [53], native defects both resident in the bulk and created by the metallization [54], processing [55], adsorbates [56, 57], sample orientation [58, 59] and presence of surface dipoles [60], can all affect the ZnO surface and the metal-semiconductor junction performance. Similar effects can account for the wide scatter, up to ~ 2 eV in the ZnO work function (i.e. $\chi_s + (E_C - E_F)$, see Fig. 3.1(a)) reported in the literature [61] since this quantity is an extremely sensitive measure of the surface state. In the appended papers I, II and IV a value of ~ 4.1 eV is used for χ_s, as measured by Coppa et al. [57] for the O-face $(000\overline{1})$

after surface cleaning by exposure to a remote O_2/He plasma at $\sim 500\ ^oC$ sample temperature. Then, the estimated Φ_b values using the Schottky-Mott model become ~ 1.5 eV for Pt, ~ 1.0 eV for Ni, Pd and Au and ~ 0.2 eV for Ti and Ag [46].

A survey of previously reported results in the literature for Φ_b on n-type ZnO is given in Table 3.1. The values of Φ_b are, in general, lower than those predicted by the Schottky-Mott theory and they do not correlate with the metal work function. In addition, the *SC*s ideality factor (n) for the current-voltage characteristics are substantially higher than unity as will be discussed more in Chapter IV. *SC*s can be accomplished by using a simple pre-cleaning of the ZnO samples in organic solvents [62, 55], but in many cases the rectifying behavior, or the improved rectification, involves some kind of more advanced surface pretreatment: in oxygen plasma [57, 54], in hydrogen peroxide [63, 64], or a $(NH_4)_2S_x$ solution [65], etching of the surface using HCl [66], or a soak in concentrated H_3PO_4 followed by a dip in HCl [37]. The use of metal oxides, like AgO, as a contact material seems also to represent a valid alternative; *SC*s with a high barrier, $\Phi_b \sim 1$ eV, and low ideality factors, $n \sim 1.0 - 1.1$, have been obtained in this case [67]. In conclusion, among the different pre-treatments proposed, the H_2O_2 treatment, the exposure to a remote O_2/He plasma and the use of AgO seem to be the most promising ones so far regarding the rectifying properties of the *SC*s.

The number of studies in the literature addressing the thermal and long term stability of *SC*s deposited to n-type ZnO is scarce. Polyakov et al. [55] reported that annealing of Au *SC*s at $\sim 100\ ^oC$ is already sufficient to cause surface reactions resulting in a near surface layer with reduced electron concentration and high density of deep defects. However, the thermal stability of Ag *SC*s seems

to be higher and these contacts withstanding up to $\sim 100\ ^{o}$C without degrading significantly [60].

Table 3.1: A survey of literature results for *SC*s on Zn and O face of *n*-type monocrystalline ZnO samples. The metal used as rectifying contact, the cleaning procedure, the sample face, n, Φ_b and the literature reference are listed. The values of Φ_b given are evaluated from the current vs. voltage characteristics except for the ones taken from Ref. [68] which are an average of the values deduced from current vs. voltage and capacitance vs. voltage characterization (see also Chap. IV)).

Metal	Cleaning	face	n	Φ_b (eV)	Ref.
Pt,Pd,Au,Ag	vacuum cleaving	not specified	not specified	~ 0.8	[51]
Cu	vacuum cleaving	not specified	not specified	~ 0.4	[51]
Au	O_2/He plasma @ 20 ^oC	O-face	1.3-3.7	0.43-0.48	[54]
Pt	O_2/He plasma @ 20 ^oC	O-face	1.01-3.45	0.40-0.42	[54]
Ir	O_2/He plasma @ 20 ^oC	O-face	1.36-1.58	0.64-0.68	[54]
Pd	Organic solvents	Zn-face	2.0	0.55 ± 0.01	[69]
Pt	Organic solvents	Zn-face	2.0	0.55 ± 0.01	[69]
Au	Organic solvents	Zn-face	1.4	0.71 ± 0.02	[69]
Ag	Organic solvents	Zn-face	1.2	0.78 ± 0.02	[69]
Pd	Organic solvents	O-face	1.2	0.59 ± 0.02	[69]
Pt	Organic solvents	O-face	1.2	0.68 ± 0.01	[69]
Au	Organic solvents	O-face	1.1	0.69 ± 0.01	[69]
Ag	Organic solvents	O-face	1.1	0.77 ± 0.02	[69]
AgO	Organic solvents and Ar/O_2 plasma	Zn-face	1.03-1.14	1.03-1.20	[67]
AgO	Organic solvents and Ar/O_2 plasma	O-face	1.04-1.10	0.98-0.99	[67]
Au	Organic solvents and O_2/He plasma at ~ 500 ^oC	O-face	1.86 ± 0.05	0.67 ± 0.05	[57]

Material	Cleaning	face	n	$\Phi_b\ (eV)$	Ref.
Pd	Organic solvents	O-face	1.4	0.75 ± 0.02	[62]
Au	Organic solvents	Zn-face	1.8	~ 0.65	[55]
Pt	Organic solvents and HCl	Zn-face	~ 1.1	~ 0.96	[66]
Pt	Organic solvents and HCl	O-face	~ 3.1	~ 0.6	[66]
Pt	Organic solvents and KrF laser in O_2 ambient	O-face	~ 1.77	~ 0.73	[70]
Pt	boiling $(NH_4)_2S_x$ for 30 s	O-face	$\sim$1.51	$\sim$0.79	[65]
Pd	Organic solvents	Zn-face	1.7-2.0	$0.63 - 0.74$	[68]
Pd	Organic solvents, tuolene and dimethilsulfoxide	similar results for both O and Zn faces	1.4-1.75	0.68-0.70	[68]
Ag	Organic solvents, tuolene and dimethilsulfoxide	similar results for both O and Zn faces	1.4-1.5	0.56-0.59	[68]
Au	Organic solvents, tuolene and dimethilsulfoxide	similar results for both O and Zn faces	~ 2	~ 0.56	[68]
Ni	Organic solvents, tuolene and dimethilsulfoxide	similar results for both O and Zn faces	~ 1.7	~ 0.62	[68]
Pd	HCl	similar results for both O and Zn faces	~ 1.4	~ 0.6	[68]
Pd	N_2O plasma	similar results for both O and Zn faces	~ 1.95	~ 0.6	[68]
Au	H_2O_2 for 1-30 min at 20-$\sim$150°C	not specified	1.15-2.89	0.35-0.65	[64]
Pt	H_2O_2 at $\sim$150°C	Zn-face	$\sim$1.15	$\sim$0.89	[63]

Chapter 4

Experimental methods

4.1 Atomic force microscopy

The surface topography and morphology of the investigated samples have been extensively studied by atomic force microscopy (AFM) run in tapping mode before and after the different treatments employed. Fig. 4.1 depicts schematically the principle of the AFM. A laser beam is incident on the cantilever and the reflected beam is directed on a four quadrant photodiode for detecting the angular displacement of the cantilever which can be moved in three spatial directions by changing the voltage applied to a piezoelectric scanner. The tip to probe the sample surface is placed at the free end of the scanner.

Three modes are commonly used for characterizing the surfaces: contact mode, no-contact mode and tapping mode. In the contact mode, the tip is kept in touch

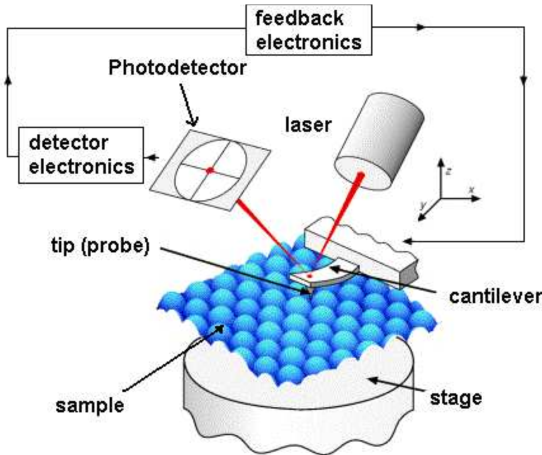

Figure 4.1: Main components of an *AFM* set-up. The cantilever support is mounted on the piezoelectric element connected to the feedback electronics to maintain a given cantilever deflection or oscillating amplitude according to the mode used for scanning the sample surface (contact or tapping/no-contact mode).

with the surface while a feedback loop maintains a constant deflection (set by the operator) between the cantilever and the sample surface. The scanner height needed for maintaining the given deflection represents the topographic image of the surface. High resolution and high speed can be obtained in this way, keeping a high constant force between the tip and the sample during the scan, but it may affect both the sample surface and the tip life-time in comparison to non-contact measurements. In detail, during contact mode surface scans, pressures on the verge of the ZnO elastic-plastic threshold equal to $\sim 10^8$ N/cm^2 [71] are usually applied [72] and can cause penetrations up to ~ 50 nm. Hence, partic-

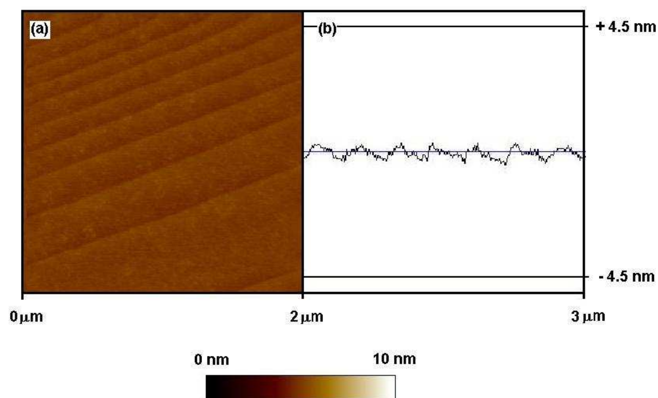

Figure 4.2: (a) ZnO O-face tapping mode amplitude images after an annealing in ZnO powder and air for 1 h at 1350 ^{o}C, in (b) a section view revealing that the steps height is $\sim 5\AA$.

ular care has to be used during the characterization of ZnO surfaces in contact mode. The non-contact mode is based on maintaining the tip oscillating with an amplitude kept constant by the feedback loop typically, a few tens of nanometers above the sample surface. Thus, in this case no force is exerted on the sample surface and only minor surface damage is expected. However, the rather weak interaction force between the sample and the tip limits the spatial resolution and lowers significantly the scan speed. In general, non-contact measurements require vacuum conditions and/or highly hydrophobic materials to achieve an acceptable signal-to-noise ratio. The tapping mode represents a compromise in between the other two in terms of resolution, scan speed, surface, and tip damaging. In this case, the cantilever is maintained oscillating at a frequency close to the resonant

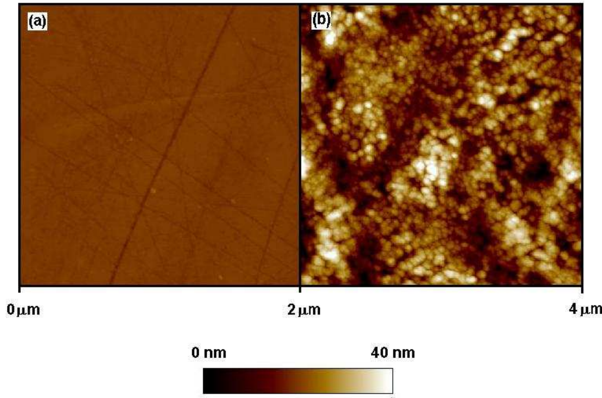

Figure 4.3: ZnO O-face *AFM* tapping mode amplitude images of (a) the as received sample (reference), (b) of a sample annealed in O_2 atmosphere for 1 h at 350 ^oC.

one, while the tip is lightly touching (tapping) the sample surface. The oscillating amplitude, monitored by the four quadrant photodiode, is kept constant at a given value, set by the operator, through a feedback loop that adjusts the voltage applied to the piezoelectric scanner. The height of the scanner necessary for maintaining the given oscillation amplitude of the cantilever is stored by the computer and forms the topographic image of the sample surface.

Different treatments for improving the surface quality and/or increasing its electron affinity before the deposition of the *SC*s have been explored by us. The effects on the O-face $(000\overline{1})$ by annealing in ZnO powder and air for 1 h at 1350 ^oC, annealing in O_2 atmosphere for 1 h at 350 ^oC, and dipping in H_2O_2 for 10 min are shown in Figs. 4.2, 4.3 and 4.4, respectively. In Fig. 4.2, atomic steps

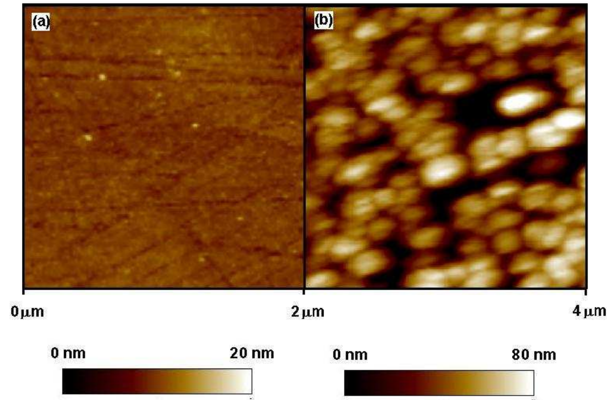

Figure 4.4: ZnO O-face tapping mode amplitude images (a) as received (b) after dipping the sample for 10 min in H_2O_2. Notice the different scale in figures (a) and (b).

with a height of approximately the unit cell length along the *c* axis occur and the root mean square (*RMS*) of the surface roughness in between the steps is $\sim 1\AA$. However, on millimeter lateral scale, this treatment causes a high density of pits ($\sim 2 \times 10^2$ mm^{-2}) with dimensions in the micrometer range both laterally and vertically. Since such defects are expected to be detrimental to *SC*s electrical performance, the procedure of high temperature annealing in ZnO powder and air has not been pursued further. Secondly, mild oxidation in O_2 atmosphere for 1 h at 350 ^{o}C has been investigated, as shown in Fig. 4.3. Despite the relatively low annealing temperature, the effect on the surface morphology is quite dramatic with an increase in the *RMS* roughness of the surface from 0.8 ± 0.3 nm up to 17 ± 4 nm. *SC*s deposited on the O-face $(000\overline{1})$ of these samples showed a modest recti-

fication up to ~ 1 order in magnitude. Thirdly, the effect of dipping the samples in H_2O_2 is illustrated in Fig. 4.4. Depending on the sample used, the *RMS* surface roughness reaches values in the range of 1.9 ± 0.3 to 22 ± 3 nm. Concurrently, a dramatic improvement in the rectification of Pd *SC*s deposited on the O-face $(000\overline{1})$ of these samples takes place. The rectification approaches values of up to ~ 9 orders of magnitude as thoroughly discussed in the appended papers I and II.

4.2 Current versus Voltage characterization

Current versus voltage $(I-V)$ measurements represent a crucial test to reveal if the deposited *SC*s are rectifying and showing the desired diode like behavior or not.
Assuming that thermionic emission holds, i.e. the emission of electrons from the semiconductor into the metal is the limiting factor for the current flow through the *SC*, the current density (J) versus applied voltage (V) behavior of a *SC*s is described by [46]:

$$J = J_0\, exp\left(\frac{e\,(V - IR_S)}{nk_BT}\right)\left[1 - exp\left(\frac{-q\,(V - IR_S)}{k_BT}\right)\right];\ \text{with}\quad I = J\,A. \quad (4.1)$$

where J_0 is the reverse saturation current density for an ideal Schottky contact, e the electron charge, I the total current flowing through the device, R_S the series resistance, n the ideality factor, k_B the Boltzmann's constant, T the absolute temperature and A the contact area. The reverse saturation current density, J_0 is related to Φ_{b0}, the zero bias barrier height, through the equation [46]:

$$J_0 = A^* exp\left(\frac{-e\Phi_{b0}}{k_BT}\right) \quad (4.2)$$

where A^* is the Richardson constant for thermionic emission and is given by

$$A^* = \left(\frac{4\pi m^* e k_B^2}{h^3} \right) \tag{4.3}$$

with h as the Plank constant.

As seen by Eq. 4.1, the total current flowing through the metal-semiconductor junction depends on the effective voltage $V_{eff} = V - IR_S$ biasing the *SC*. In order to be estimated V_{eff} R_S has to be known. Considering the $I - V$ characteristic of a *SC* under forward biases with $V - IR_S \gg k_B T$, the following equation can be derived:

$$G = \frac{\partial I}{\partial V} = \frac{\partial}{\partial V} \left(A\, J_0\, exp \left(\frac{e\,(V - IR_S)}{nk_B T} \right) \right) = I \frac{e}{nk_B T} (1 - GR_S) \tag{4.4}$$

where G is the contact conductance. Hence, a linear fit of G/I versus the conductance G yields both n and R_S if the appropriate range is considered [73]. Once R_S is determined, the applied voltage V can be corrected for the voltage drop over R_S and V_{eff} is obtained. Then the ideality factor n can be evaluated for the whole range of applied biases by considering that:

$$n = \frac{eV_{eff}}{k_B T} ln \left[\frac{J_0 \left[1 - exp \left(\frac{-q(V_{eff})}{k_B T} \right) \right]}{J} \right]. \tag{4.5}$$

The analysis of a *SC* according to the described procedure is shown in Fig. 4.5(a), (b), (c) and (d); in (a) an acquired $I - V$ characteristic is displayed, in (b) the G/I vs. G dependence for determining R_S is illustrated, in (c) the measured I is plotted against V_{eff} and in (d) the dependence of n on V_{eff} is shown. It is worth to notice that the ideality factor, n, is introduced for taking into account the first order dependence of Φ_b on the voltage V and n should be constant when V is

varied. Moreover, in addition to an insulating layer between the metal and the semiconductor, also image force lowering, i.e. the lowering of the energy barrier the electrons have to overcome because of charge screening induced by electrons that are crossing the depleted region in the metal contact, is a mechanism introducing a dependence of Φ_b on V. A typical increase in n from 1, its ideal value, up to ~ 1.02 is expected due to image force lowering in ordinary forward biased *SC*s [46]. However, other mechanisms, like recombination in the space charge region or tunneling through the barrier, can also cause apparent deviations of n from unity. Therefore, the main phenomena yielding a voltage dependence of Φ_b can usually not be directly elucidated from ordinary $I-V$ characterization.
In our case, all the *SC*s measured (see also attached papers I, II and IV) displayed the behavior shown in Fig. 4.5(d), with n close to unity (ideal value) at reverse bias and a substantial increase as the *SC* is forward biased. The latter suggests a rather strong dependence of the barrier height on the applied voltage during forward biasing. As discussed in chapter 3, high ideality factors are quite common for Schottky contacts to n-type ZnO and mechanism like tunneling through the Schottky barrier, the presence of interface states and the influence of deep recombination centers have been proposed (see [55, 74] and references therein). Further, such high values of n as shown in Fig. 4.5(d) imply that the current transport through the *SC* can not be properly described as purely thermionic and hence, an evaluation of the Schottky barrier height using $I-V$ measurements only is not valid. Therefore, also capacitance versus voltage measurements $(C-V)$ have been extensively used in this thesis.

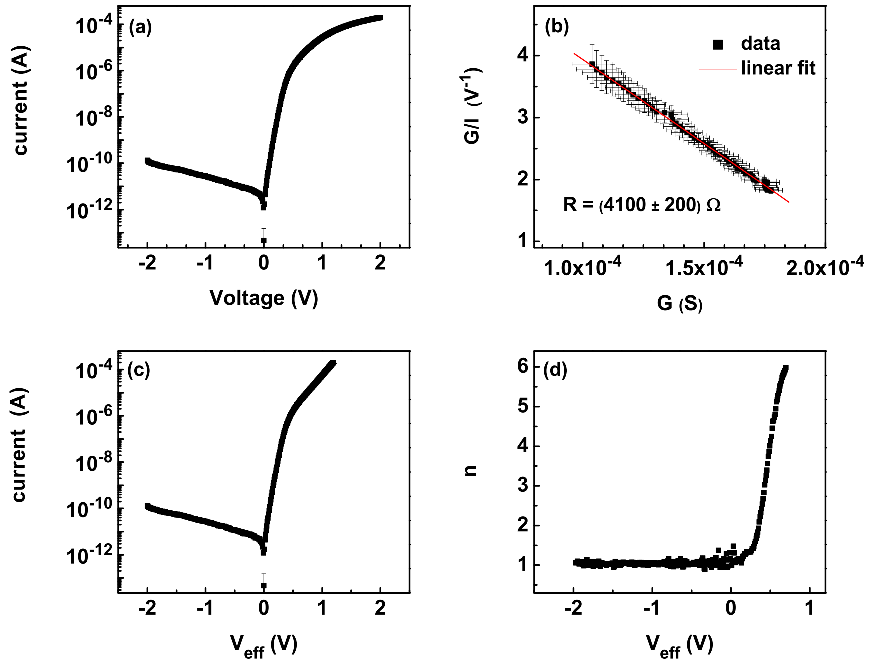

Figure 4.5: (a) An $I-V$ characteristic as acquired for Pd *SC* on *n*-type ZnO. (b) The G/I vs. G dependence for determining R_S, a value of $(4100 \pm 200)\Omega$ is extracted for R_S in this case. (c) An $I-V$ characteristic vs. the effective voltage bias applied to the metal semiconductor junction, that is $V_{eff} = V - IR_S$. (d) the ideality factor n dependence vs. V_{eff}. All the experimental data shown are for the same *SC* after it has been annealed at 200 ^{o}C for 30 min.

4.3 Capacitance versus Voltage characterization

Capacitance versus voltage measurements $(C-V)$ are commonly used for electrical characterization of *SC*s as well as of the semiconductor material itself. Thus

$C-V$ measurements have been employed both for determining the concentration vs. depth of electrons that are responding to the probing signal at room temperature and Φ_b, that, hereafter, will be labeled as Φ_b^{CV}.
The concentration profile of electrons (N_{eff}) responding to the probing signal of frequency f_T at a depth W is given by [75]:

$$N_{eff}(W) = \frac{1}{e\,\varepsilon_0\,\varepsilon_r\,A^2} \frac{C^3}{\frac{\partial C}{\partial V}} \tag{4.6}$$

with

$$W = \frac{\varepsilon_0\,\varepsilon_r\,A}{C} \tag{4.7}$$

where C is the depletion capacitance.
N_{eff} extracted from the $C-V$ characterization accounts for the total amount of electrons responding to the probe signal, including contribution from both shallow donors N_d and defects with levels deeper into the band-gap, Di. The effect of Di on the C measurements depends on the magnitude of the probe frequency f_T and sweep frequency of the applied driving voltage respect to the time constant of the Di charging-discharging process. Assuming that Di interacts with the conduction band, as the samples studied are of n-type semiconductor, this time constant can be expressed as [75]:

$$e_n^{Di} = \sigma_{Di}\,T^2\,\gamma\,exp\,(\frac{-E_{Di}}{k_B T}) \tag{4.8}$$

with

$$\gamma = 2\sqrt{3}\,(2\pi)^{\frac{3}{2}}\,k^2 \frac{m\,m^*}{h^3} \tag{4.9}$$

where E_{Di}, σ_{Di} and h are the defect activation energy, capture cross section modified for the degeneracy ratio, and, the Plank constant, respectively and e_n^{Di} describes the rate the electrons are emitted from the Di defects into the conduction band.

For a n-type semiconductor with a uniform concentration N_d and N_a of shallow donors and compensating acceptors, respectively, and negligible Di, the capacitance C is related to the built in voltage V_{bi} (see Fig. 3.1 and 3.3) according to [46]:

$$C^{-2} = \left(\frac{2}{A^2 e\,(N_d - N_a)\varepsilon_0\varepsilon_r}\right)\left(V_{bi} + V_r - \frac{k_B T}{e}\right) \tag{4.10}$$

and then $C - V$ measurements can be used to establish Φ_b^{CV} considering that [46]:

$$\Phi_b^{CV} = V_I + \frac{kT}{e} + (E_C - E_F) \tag{4.11}$$

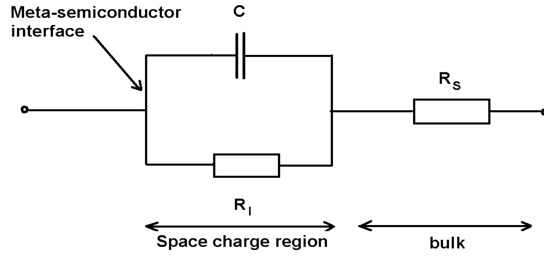

Figure 4.6: *SC* equivalent circuit. The space charge region below the *SC* is modeled as the depletion capacitance C in parallel with a leakage resistance R_I, while the bulk is contributing to the total device impedance with the series resistance R_S.

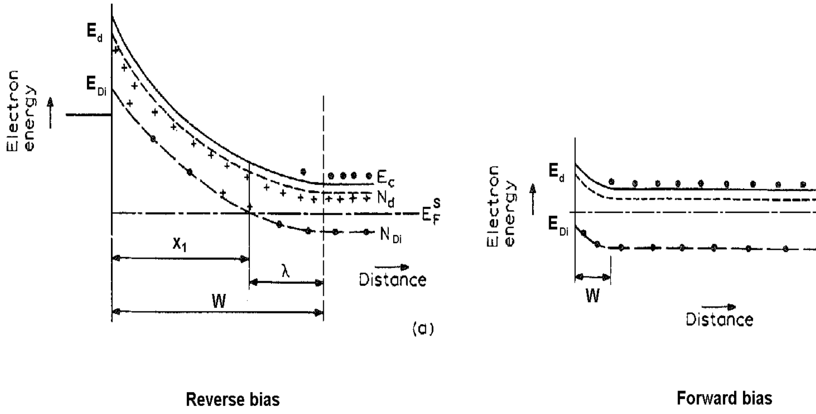

Figure 4.7: Band diagram of the space charge region when a reverse bias (a) and a forward bias (b) are applied, respectively. In case of reverse biasing, the *Di* levels are fully occupied where E_F^S is higher than E_{Di} and completely empty closer to the metal-semiconductor interface where, due to the band bending E_F^S is below E_{Di}. On the other hand, by applying a forward biasing, the E_{Di} levels can be pushed below E_F^S through the whole space charge region. In this case, the *Di* centers, if assumed donor-like defects, are not contributing to the measured capacitance since all neutral.

where V_I is the intercept with the abscissa when plotting $1/C^2$ against V.

Here it should be emphasized that, in general, the presence of deep defects Di responding to the probing signal, but not included in N_d, can contribute, to the measured charge beside N_d and N_a and, consequently, affect the Φ_b^{CV} estimate. In detail, as shown in Fig 4.7(a) due to the band bending E_F^S crosses E_{Di} at a distance $x_1 = W - \lambda$ from the metal semiconductor junction, then for a depth less than x_1

the Di levels, assumed donor-like, are ionized, hence contributing to the charge distribution in the depleted region. Moreover, in case $f_T \ll e_n^{Di}$, the oscillations of E_F^S driven by the probing signal are charging and discharging the Di defects placed $\approx x_1$ that, in this case, contribute to the measured fluctuations in the space charge as well. However, even when $f_T \ll e_n^{Di}$ both these contributions related to the presence of the Di defects can be minimized by forward biasing the SC. In this case, the Di levels can be pushed down below E_F throughout the whole depletion region, as shown in Fig. 4.7(b), resulting all neutral and not affecting the measured capacitance that is exclusively depending on N_d and N_a. Therefore a comparison of the near surface N_{eff} extracted from the $C-V$ characterization with the expected carrier concentration n, expected to be equal to $N_d - N_a$, can be used to establish if the Di are contributing significantly to the measured C. Hence, the C measurements taken in forward bias, corresponding to probing the material near to the metal-semiconductor junction are of particular importance if an accurate analysis has to be done.

A SC is commonly described by the equivalent circuit shown in Fig. 4.6, where the actual measurements are normally made assuming a negligible contribution of R_S to the measured values of C and R_I. However, this assumption it is not always valid for the whole forward biasing range since, at some point, with increasing current flow $R_I \sim R_S$. Hence, particular care has to be taken to establish the maximum forward voltage that can be applied without affecting significantly the measured values of C and R_I. The validity of the measured C values has been confirmed by requiring the fulfillment of the following criteria [75]:

$$R_S \ll R_I \tag{4.12}$$

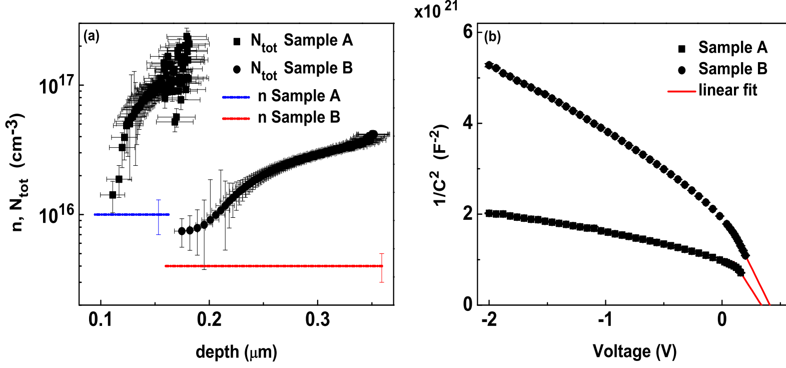

Figure 4.8: (a) An example of N_{eff} profiles in the (0001) direction for two representative samples A and B. In the same graph the free carrier concentration, n, as determined by TDH measurements at room temperature is included for comparison. (b) The $C^{-2}-V$ curves and their linear extrapolations to determine V_I. Both the $C^{-2}-V$ characteristics and N_{eff} are obtained with f_T equal to 1 kHz.

$$2\pi f_T C R_S \ll 1 \tag{4.13}$$

$$V R_S \frac{\partial (R_I)^{-1}}{\partial V} \ll 1 \tag{4.14}$$

where R_S is the series resistance evaluated from the $I-V$ characterization, as previously described.

Upper limits of 5 $^0/_{00}$, 10 $^0/_0$ and 5 $^0/_{00}$ for the criteria 4.12, 4.13 and 4.14,

respectively have been used yielding an overall error of $\lesssim 2\ ^0/_0$ for the measured values of N_{eff} [75].
An example of N_{eff}, extracted according to these criteria, is displayed in Fig. 4.8(a), where N_{eff} is compared with the free electron concentration, n, determined by TDH measurements performed at 290 K. Within the experimental accuracy the near surface the values of N_{eff} are in reasonable agreement with n suggesting strongly that Di is responsible for the loss in responding electrons towards the surface. Furthermore, evaluation of the $1/C^2$ data against V by using only the measurements taken under forward bias, as shown in Fig. 4.8(b), yields Φ_b^{CV} equal to ~ 0.52 and ~ 0.62 eV for sample A and B, respectively, which appear as realistic values.

4.4 Thermal admittance spectroscopy

The thermal admittance spectroscopy, *TAS*, is a characterization method [75, 76, 77, 78] based on the changes in the *SC* capacitance (C) and conductance (G) with the sample temperature related to the temperature dependence of the e_n^{Di} for the Di present in the depletion region.
From the *TAS* spectra activation energies (E_{Di}) of levels that are crossing E_F within the space charge region can be extracted. In addition, if V_{bi}, E_F and N_{eff} are known the defect concentration (N_{Di}) and capture cross section (σ_{Di}) can be determined as well, according to the theory hereafter summarized.

4.4.1 Above the freeze out temperature of the charge carriers

The general expression of the small signal admittance of a *SC* containing multiple deep levels has been reviewed in detail by Beguwala et al. [79] and the relationship between the defect properties and the resulting *SC* admittance is not straightforward. However, in case every transition between the occupied and unoccupied states in the space charge region can be attributed unambiguously to one defect at the time then the truncated space charge approach [80, 81] can be used and the one level system analysis can be applied with minor corrections. Therefore, the following description is limited to the presence of just one deep level $D1$ beside the shallow donor with an effective concentration N_{eff}.

In this case, an abrupt transition between the occupied and unoccupied $D1$ states can be assumed to occur where, due to the band bending, the emission and capture rate from D_1 are equal [76, 75]:

$$\Delta_{D1} = \frac{(E_F + k_B T \; ln\, 2 - E_{D1})}{e} = 0 \tag{4.15}$$

where a degeneracy of 1 and 2 in case the level $D1$ is empty and singly occupied, respectively is assumed. It can be noticed that, in the present case, the condition $\Delta_{D1} = 0$ is fulfilled at a distance $\sim x_1$ in the space charge region (see Fig. 4.7(a)) considering the temperature range of the taken *TAS* measurements. When $f_T \ll e_{D1}$ the defects located around x_1 will respond to the probing signal, providing a charge change in phase with the driving voltage, i.e., contributing to the measured capacitance at high temperature C_{HT}. On the other hand, while the temperature is decreased the D_1 defects will start to lag behind the probing signal determining a decrease in the capacitance from C_{HT} to C_{LT}, where the latter is the low temperature limit. From the step in the capacitance $\Delta C = C_{HT} - C_{LT}$, if E_F,

V_{bi} and N_{eff} are known, then N_{D1} can be evaluated according to the equation [76]:

$$\alpha = \frac{-(B+1) + \left((B+1)^2 + 4\,B\,(F-1)\right)^{\frac{1}{2}}}{2\,(F-1)} \tag{4.16}$$

with

$$\alpha = \frac{N_{D1}}{N_{D1} + N_{eff}} \tag{4.17}$$

$$B = \frac{V_{bi} + V_r}{\Delta_{D1}} \tag{4.18}$$

$$F = \frac{\left(\frac{\Delta C}{C_{HT}} - 1\right)^2}{\left(\frac{\Delta C}{C_{HT}}\right)^2} \tag{4.19}$$

where V_r is the absolute value of the applied reverse bias and a uniform concentration for both N_{eff} and N_{D1} is assumed.

Furthermore, assuming that in the temperature range where the step in C is occurring, the change in the width of the depleted region, W, is negligible, then the capacitive step is expected to be joined by a maximum peak amplitude in the $G/2\pi f_T$ versus temperature spectrum, $\left(\frac{G}{2\pi f_T}\right)_{max}$, equal to $\frac{\Delta C}{2}$ with both $\Delta C/2$ and $(G/2\pi f_T)_{max}$ occurring at the same temperature T_{max} and with an amplitude independent on f_T [75]. This temperature, T_{max}, is related to E_{D1} according to the equation [76]:

$$\frac{2\pi f_T}{T_{max}^2} = 2\left(\frac{1-A}{1-\alpha}\right)\sigma_{D1}\,\gamma\,exp\,(\frac{-E_{D1}}{k_B T_{max}}) \tag{4.20}$$

with

$$A = \left(\frac{\Delta C}{C_{HT}} \right) \tag{4.21}$$

and where σ_{D1}, the capture cross section modified for the degeneracy ratio, is assumed to be independent on the temperature and where the entropy change possibly occurring during the emission process is considered to be negligible. Hence, an Arrhenius plot of ω_T/T_{max}^2 versus T_{max}^{-1} yields E_{D1} directly prior to determine N_{D1} and σ_{D1} in case both α and A can be assumed constant in the temperature range of interest.
The same calculation can be applied in case more levels are present if an effective voltage [76] $(V_B + V_r)^*$ is introduced to take into account the effect of the levels not responding to the probing signal, but still affecting W.
An example of the capacitive part of *TAS* spectra is shown in Fig. 4.9(a). For this sample three levels are revealed; a shallow one, D_2, responsible for the freeze out step, an intermediate level, D_X, with an unexpected dependence of the step height on T_{max} and f_T and a more deeper one, D_3. For the latter one, Fig. 4.9(b) shows an activation energy of (0.29 ± 0.03) eV. In addition, applying the theory described above N_{D3} and σ_{D3} become equal to $(2 \pm 1) \times 10^{16}$ cm^{-3} and $(6 \pm 3) \times 10^{-15}$ cm^2, respectively if the values of $\sim 4 \times 10^{15}$ cm^{-3} and ~ 0.4 eV are used for N_{eff} and V_{bi}, respectively. However, in case of D_X the theory is not straightforward to use since, as mentioned above, the C step height is expected to depend on neither T_{max} nor f_T. As discussed thoroughly in paper IV, this behavior is attributed to the negative-U character of the D_X defect.

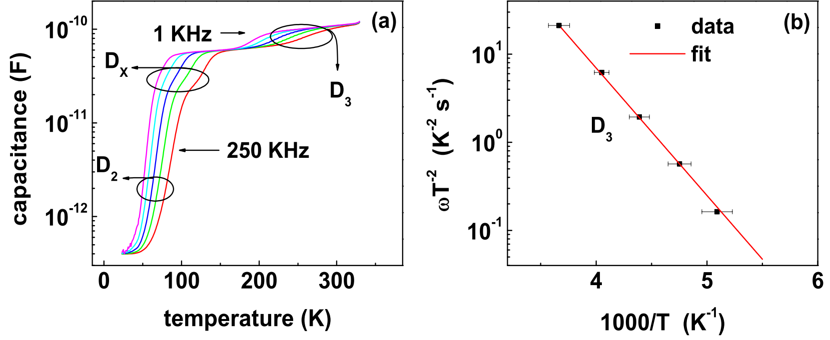

Figure 4.9: (a) An example of $C-T$ spectra in case of a sample showing three main levels labeled as D_2, D_X and D_3. (b) The Arrhenius plot for the level D_3 evaluated according to the theory summarized in this section.

4.4.2 The freeze out region of charge carriers

In the freezing region the bulk carrier concentration, due to the main donor level, decreases and causes a progressive increase in R_S (cf. Fig. 4.6). Hence, at sufficiently low temperature, the final capacitance, C_G will be independent on the applied bias and equal to the geometric capacitance of a capacitor with the semiconductor acting as an insulator between its contact plates, $C_G = \varepsilon_0 \varepsilon_r A/t$ where t is the thickness of the sample. The starting equivalent circuit for the *SC*, in this case, is obtained by substituting R_S (see Fig. 4.6) with a series of slices each acting as capacitor in parallel with a resistor to model the not depleted bulk region [82].

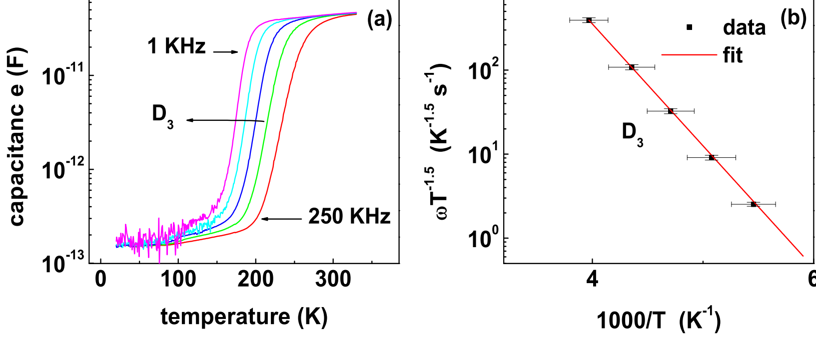

Figure 4.10: (a) An example of $C-T$ spectra in case of a sample where D_3 represent the main donor level on which the free carriers are freezing out. (b) In this case the Arrhenius plot for the level D_3 has been evaluated considering a constant mobility in the temperature range the freezing out is occurring.

Hence, indicating with ρ the material resisitivity and δx the width of the slices, the total *SC*'s impedance is obtained by adding to the space charge region impedance the capacitive and resistive contribution of each slice equal to $\varepsilon_0 \varepsilon_r A/\delta x$ and $\rho\delta x/A$, respectively. On the basis of the previous model, it can be demonstrated that $\left(\frac{G}{2\pi f_T}\right)_{max} = \frac{\Delta C}{2}$ still holds. Furthermore, in this case, it is shown that T_{max} is related to f_T according to the following equation [76]:

$$\frac{f_T}{\mu(T_{max})\, T_{max}^{3/2}} \propto exp\,(\frac{-E_d}{kT_{max}}) \tag{4.22}$$

Hence, for determining the temperature dependence of the right hand side of Eq. 4.22 the mobility vs. temperature dependence has to be known. In general, a power law of the kind $\mu_0 \, T^b$ can be assumed, where the exponent b is chosen according to the dominant scattering mechanism in the temperature range where the freezing out occurs. For the sample investigated in Fig. 4.10(a), the D_3 defect represents the main donor providing the free carriers and its position in the band gap can be established. Furthermore, considering that the freezing out takes place at the temperature where the mobility maxima have been observed by temperature dependent Hall effect measurements performed on the same sample prior to the *SC*s deposition, b is put equal to 0 in Fig. 4.10(b). An activation energy of (0.29 ± 0.03) eV is extracted, in agreement with that determined for the sample displayed in Fig. 4.9(b), where D_3 is not the most shallow donor. The resulting E_{D3} and σ_{D3} values extracted in these cases are consistent with those of the so called E_3 defect, frequently reported in the literature [34, 83].

4.5 Temperature dependent Hall effect

Temperature dependent Hall effect(TDH) measurements represent a characterization technique that can be used to determine the mobility of carriers, μ , and their concentration, n, in semiconductors. In addition, from the carrier concentration vs. temperature dependence it is possible to deduce both the concentration and activation energies of the main donors and acceptors. Moreover *SCs* are not needed to perform the TDH characterization and at least in case of ZnO this is an advantage since high quality Ohmic contacts are accessible and have been reported by a number of groups [15]. On the other hand, results extracted from

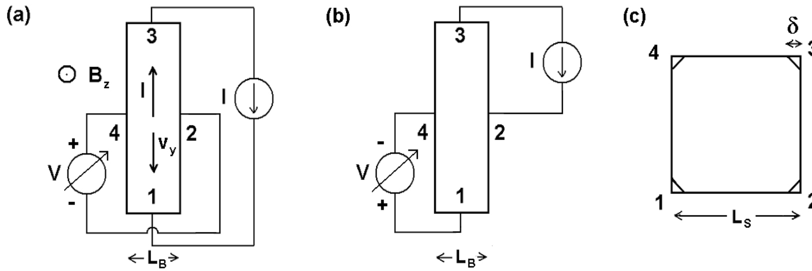

Figure 4.11: (a) Schematic to illustrate the principle of the Hall effect measurement in case of a bar. The numbers are labeling the Ohmic contacts needed to probe the sample. In (b) the connection configuration in case the resistivity is measured. In (c) the sample and Ohmic contacts geometry used during this work of thesis is shown.

TDH measurements represent an integral average over the whole sample, while from other techniques employing *SC*s, like admittance and deep level transient spectroscopy, information on the spatial distribution of the levels can be deduced as well.

4.5.1 Basic relationships

In Fig. 4.11(a) a schematic of the Hall measurement on a bar is shown. In the following description the bar and the contacts are assumed to be uniform and Ohmic, respectively; moreover the impedance of the voltmeter to measure the voltage drop is considered high enough not to perturb the uniform voltage drop along the bar. In case of a n-type material, the current I forced to flow from contact 1 to 3, constitutes mainly of electrons moving in the opposite direction and due the

presence of an uniform magnetic field B_z, orthogonal to the picture plane, they are deflected from the side of contact 4 towards the opposite side of contact 2 because of the Lorentz force. A steady state is reached when the Lorentz force equals the electric field produced by the charge excesses present on these two sides. Then, the following equation holds:

$$(V_4 - V_2)_{B=B_z} - (V_4 - V_2)_{B=0} = V_H = ev_y B_z L_B = \frac{IB_z}{n_H\, t} \tag{4.23}$$

where v_y, I, n_H and t are the electron drift velocity, the current, the Hall concentration of electrons and the bar thickness, respectively, while L_B is the bar lateral dimension. The difference between the voltage drop $(V_4 - V_2)_{B=B_z}$ when the magnetic field is equal to B_z and with no magnetic field, $(V_4 - V_2)_{B=0}$ is taken to minimize the effects of possible misaligments between the contacts 4 and 2.
Hence, by measuring the Hall voltage, V_H, n_H can be determined. In addition, by exchanging the role of two contacts, as shown in Fig. 4.11(b), the van der Pauw method [75] can be used to measure the sample resisitivity, ρ according to [75]:

$$exp\left(-\frac{\pi\, t(V_1 - V_4)}{I\, \rho}\right) + exp\left(-\frac{\pi\, t(V_4 - V_3)}{I\, \rho}\right) = 1 \tag{4.24}$$

where $V_4 - V_3$ is the voltage drop between contact 4 and 3 when the current in injected into contact 1 and extracted from contact 2, while $V_1 - V_4$ is measured as depicted in Fig. 4.11(b).
Considering that ρ is related to the Hall electrons' mobility, μ_H, according to the equation $\rho = (e\, n_H \mu_H)^{-1}$, then μ_H can be determined as well. Finally, both the actual carrier concentration n and the drift mobility can be extracted using the expressions $n = n_H r_H$ and $\mu = \mu_H / r_H$, respectively, with r_H being the Hall scattering factor [1, 75] introduced to consider the energy distribution of the electrons

not taken into account in the above argument, where all electrons are assumed to move with a velocity v_y.
It is worth to be noticed that both Eqs. 4.23 and 4.24 hold, indeed, independently of the sample shape if the material is uniform and the measurements are made through line contacts placed on the edges, as demonstrated by van der Pauw [75]. Hence, flexible sample shapes can be used for performing the Hall characterization. In addition, it is standard practice to reverse the current and magnetic field and interchange the contacts for voltage measurement and current injection to minimize the effects of possible thermomagnetic effects that could falsify the results.
For the measurements in this thesis, averaging to reduce thermomagnetic effects was performed, and square-shaped samples with Ti/Al/Pt/Au multilayer (each 200 $\AA$ thick) triangular Ohmic contacts deposited at the corners, as shown in Fig. 4.11(c), were used. The effects caused by a finite contact size were accounted for in the data analysis, of paper III, following the procedure outlined by Chwang et al. [84].

4.5.2 The procedure used in analyzing the Hall data

The analysis of the Hall data has been performed using a code written in Matlab® to simulate both the measured $n_H(T)$ and $\mu_H(T)$. The concentration of electrons in the conduction band n is given by the equation [85]:

$$n(T) = \frac{1}{4}\left(\frac{2m\, m^* k_B T}{\pi\hbar^2}\right)^{\frac{3}{2}} e^{-\left(\frac{E_C(T)-E_F}{k_B T}\right)} \tag{4.25}$$

where $E_C(T)$ is the band gap energy relative to the valence band edge with the variation of E_C with T given in Table 2.1. On the other hand, E_F, needed to

calculate n from Eq. 4.25 to be compared with the measured $n_H(T)$, is obtained by solving the charge neutrality condition:

$$n + \sum_i N_{Ai}^- = \sum_i N_{Di}^+ + p \tag{4.26}$$

with [85]:

$$N_{Di}^+ = N_{Di} \frac{1}{1 + 2\, e^{-\left(\frac{E_C(T) - E_{Di} - E_F(T)}{k_B T}\right)}} \tag{4.27}$$

where p is the overall hole concentration in the valence band, N_{Ai}^- is the ionized acceptor concentration of type Ai that are providing the compensation, all of them considered fully ionized, N_{Di} and N_{Di}^+ are the total and ionized concentration of donors of type Di. In detail and, as described in paper III, the measured $n_H(T)$ temperature dependence has been modeled assuming the presence of a fully ionized single charged acceptor (A) and three s-like donors (Di, $i = 1,2,3$) with energy levels E_{Di} extracted independently (see paper IV) by TAS measurements performed on the same samples. Arbitrary starting values for N_A^- and N_{Di}, with $i = 1,2,3$ and r_H equal to 1, are chosen for performing the first fit of the measured n_H and an estimate of N_{Di} and the related quantities N_{Di}^0 and N_{Di}^+ are extracted. Then the fit of the mobility data is performed using the relaxation time approximation (RTA). The RTA approach [75, 1] is based on the assumption that each scattering process (j) affecting the carrier mobility is uncorrelated and can be described by a relaxation time $\tau_j(E)$ that may depend on the carrier energy E. Therefore, in this approximation, the total relaxation time for a carrier with energy E ($\tau_{tot}(E)$) is deduced from $\tau_{tot}(E) = (\sum_j 1/\tau_j(E))^{-1}$ (Matthiesen's rule). Once $\tau_{tot}(E)$ is known both μ and r_H can be evaluated according to: [1, 75]

$$\mu = \frac{e}{m\,m^*}\left(\int_0^{+\infty} \tau_{tot}(E)\, E^{\frac{3}{2}}\, e^{-\frac{E}{k_B T}}\, dE\right) \tag{4.28}$$

and

$$r_H = \frac{<\tau_{tot}^2>}{<\tau_{tot}>^2} = \frac{\int_0^{+\infty} \tau_{tot}^2(E)\, E^{\frac{3}{2}}\, e^{-\frac{E}{k_B T}}\, dE}{\left(\int_0^{+\infty} \tau_{tot}(E)\, E^{\frac{3}{2}}\, e^{-\frac{E}{k_B T}}\, dE\right)^2}. \tag{4.29}$$

The neutral and ionized impurities, dislocations, acoustic deformation, piezoelectric and polar optical potentials have been included as scattering centers during the analysis of the measured data. According to the detailed description of their expressions given in paper III, these scattering contributions are fully determined by using the ZnO constant reported in Table 2.1, the N_{Di}^0 and N_{Di}^+ previously determined as fixed parameters and N_A^- as a fitted value. In this case, the calculated mobility is directly compared with the measured one after the correction by r_H obtained during the same fitting step. The estimates of N_A^- and r_H obtained are, then, used as constraints for starting a new fitting cycle, i.e. to correct the carrier concentration measured accordingly and determine a better estimate of $N_{Di=1,3}$. This procedure has been iterated until consistent results are obtained from both the carrier concentration and mobility vs. temperature analysis. An example of this procedure is shown in Fig. 4.12. The best fit of the measured n and μ shown in Fig. 4.12(a) and (c) respectively, has been obtained with $N_{D1} = (1.2 \pm 0.4) \times 10^{17}$ cm^{-3}, $E_{D1} = (0.03 \pm 0.01)$ eV, $N_{D2} = (1.5 \pm 0.1) \times 10^{17}$ cm^{-3}, $E_{D1} = (0.05 \pm 0.01)$ eV, $N_{D3} = (0.4 - 4) \times 10^{17}$ cm^{-3}, $E_{D3} = (0.29 \pm 0.03)$ eV and $N_{A^-} = (2.6 \pm 0.4) \times 10^{17}$ cm^{-3}. In addition, Fig. 4.12(b) and (d) show the dependence on temperature of both E_F and $E_{Di=1,3}$ with respect to E_C and $r_H(T)$ extracted from the data, respectively.

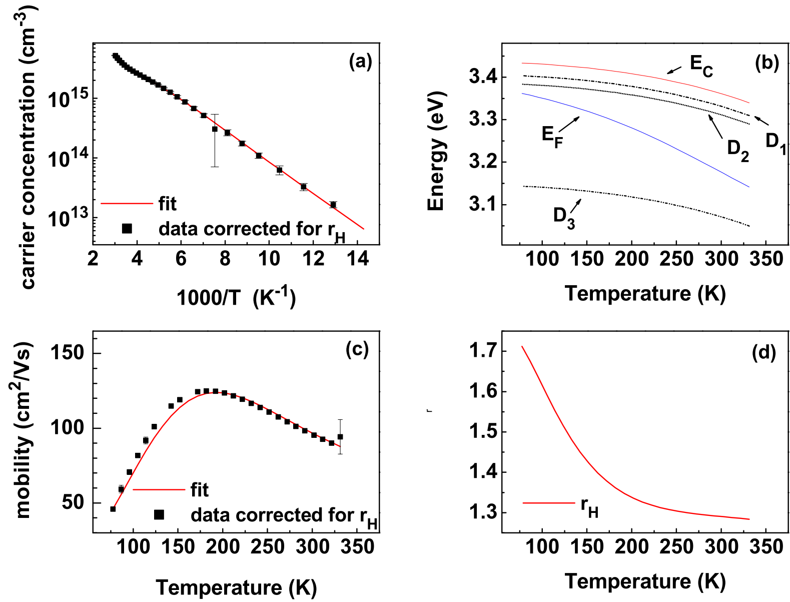

Figure 4.12: (a) The measured carrier concentration (squares) corrected for r_H and the best fit to it (solid curve). (b) The E_F vs. temperature as determined by the fitting of the experimental data and, for comparison, E_C and the position of the three main levels E_{D1}, E_{D2} and E_{D3} used to fit the TDH measurements are shown. (c) The measured mobility (squares) corrected for r_H and the resulting fitting curve (solid curve). (d) The dependence of r_H on the sample temperature.

Chapter 5

Summary of the results, conclusions and suggestions for further studies

In this chapter the main results of the papers attached are described and some suggestions for further studies based on these findings are exposed. Paper I and II describe the results of the electrical characterization of the *SCs* realized according to the procedure developed during the thesis and its effects both on the surface morphology, electrical characteristics and *SC* interface chemical properties. Papers III and IV deal more with the characterization of the material defects and the role of group I and III impurities in hydrothermally grown ZnO. Finally paper V shows an alternative procedure to realize *SC*s to ZnO based on using highly resistive material and accomplish the *n*-type doping by H implantation with no need of any pretreatment prior to the *SC*s deposition beside ordinary organic solvents cleaning.

5.1 Paper I

Different pretreatments prior the deposition of the *SC*s have been investigated: cleaning in organic solvent, in H_2O_2 and in 5% HCl diluted in deionized water (DI), in and ex situ annealing in O_2 at 350 ^{o}C, annealing in ZnO powder or air in the 950-1350 ^{o}C range, surface sputtering in Ar atmosphere, exposure of the sample surface to K_2O and Cl vapours as well as Ag and Pd as *SC*s metals. In all cases, the *SC*s were deposited on the O-face $(000\overline{1})$ sample surface. It has been found that *SC*s with good and reproducible characteristics can be achieved by pre-cleaning the samples with Aceton and then Methanol for 5 min in ultrasonic bath followed by a 15 min in total dip in H_2O_2 using Pd as contact metal. Paper I deals mainly with the effects of this pretreatment on the morphology of the O-face $(000\overline{1})$ investigated by AFM running in tapping mode and on the electrical characteristics of the resulting *SC*s and the material using $I-V$, $C-V$ and TAS measurements. The effect of the H_2O_2 pretreatment on the O-face $(000\overline{1})$ results in an increase in the surface roughness up to (2.3 ± 0.2) nm from a starting value of ~ 1 nm. Despite this increase in the surface roughness, the *SC*s deposited on the H_2O_2 treated surface exhibit up to 9 orders of magnitude in rectification in the voltage range of -2 to +2 V, which is among the highest reported for ZnO. In contrast, the reference samples cleaned with Aceton and then Methanol for 5 min in ultrasonic bath with a final dip in *DI* water show an Ohmic behavior. In addition, the effect of mild annealing at 200 ^{o}C in air for 30 min is investigated. The majority of the *SC*s measured immediately after the annealing display either stable or improved rectification ratio, but fluctuations in time are occasionally observed indicating changes at the Pd/ZnO interface or on the bare O-face $(000\overline{1})$. Despite these changes in the $I-V$ characteristics, the *SC*s still exhibit up to 7

orders of magnitude in current rectification in the -2 to +2 V voltage range after 80 days. Finally, from the electrical characterization of the *SC*c an ideality factor of $\sim$ 1.8 at a forward bias of +0.5 V is extracted suggesting that carrier recombination, tunneling and/or an interfacial layer are present.

5.2 Paper II

To investigate in more detail the effects of the H_2O_2 pretreatment on the bare O-face $(000\overline{1})$ and on the Pd/ZnO interface a combined analysis by X-ray photoelectron spectroscopy (*XPS*) and electrical measurements has been performed in paper II. Here it is shown that both room temperature $I-V$, taken by contacting the H_2O_2 ZnO O-face $(000\overline{1})$ with a probing tip, and *XPS* measurements indicate the creation of a highly resistive surface layer. On the basis of the *XPS* results, the thickness of this layer can be estimated to $\sim$ 30 $\AA$ and is attributed to excess of Oxygen as a consequence of the H_2O_2 pretreatment, as indicated both by the increase in the $[O]/[Zn]$ ratio from $\sim$ 1.0 to $\sim$ 1.1 and changes in the higher binding energies O1s peak at $\sim$ 532 eV. In addition, the *XPS* characterization of the Pd/ZnO interface reveals that the H_2O_2 pre-treatment, due to the O rich surface, is promoting the formation of PdO at the interface. Considering that theory suggests that the O terminated PdO work function is significantly higher than that for Pd (5.12 eV), both the formation of the highly resistive layer, that causes upward energy band bending and suppresses the surface leakage current, and the higher work function of PdO are suggested as possible causes of the improved performance of *SC*s to H_2O_2 treated ZnO. In addition, in paper II an estimate of 0.6 eV for Φ_B^{CV} is extracted from $C-V$ characterization and TDH measurements.

5.3 Paper III

The results obtained by a combined sample analysis using TAS, TDH and secondary mass spectrometry ($SIMS$) are described in paper III. The combination of these characterization techniques gives further insight into the defects and impurities present in hydrothermally grown ZnO. The results disclose the existence of three donor-like defects, two shallow and one deep, and a substantial concentration of fully occupied acceptors in the lower part of the energy bandgap. In detail, it is found that Al is providing a dominant contribution to a level $\sim 60-70$ meV below E_C. On the other hand, contributions from Ga and In that are giving rise to levels, according to photoluminescence (PL) measurements, close to that of Al are ruled out. It is worth to notice that this estimate of the energy level position for Al is consistent with PL data in the literature, but $\sim$ 10 meV lower than previous estimate by TDH. In addition, the role of Li is addressed: it accounts only from $\sim$40% to $\sim$70% of the concentration of compensating centers and hence, the Li content is not sufficient to account for all the acceptors observed. Additional impurities, excluding group I elements which are shown to have negligible concentrations, and/or intrinsic defects are thus of crucial importance as compensating centers in virgin hydrothermally grown ZnO. Finally, in this work the measured mobility vs. temperature dependence is analyzed in the RTA approach. This analysis reveals that the neutral scattering, due the high fraction of non-ionized deep donors ($\sim$ 0.3 eV below E_C), is a pronounced contribution to the total scattering and comparable to the piezolelectric field one.

5.4 Paper IV

Paper IV presents a comprehensive description of the *TAS* results obtained for as-grown hydrothermal samples. The analysis of the levels is performed in detail distinguishing between peaks occurring in the freeze-out region and at higher temperatures. Beside three well-behaved levels with activation energies of ~ 30, ~ 50 and ~ 290 meV, respectively consistent with the *TDH* measurements performed on the same samples prior to the *SC*s, a fourth one, D_X, placed ~ 80 meV below E_C and with σ_{DX} equal to $\sim 6 \times 10^{-17}$ cm^2 is detected. The D_3 peak shows an anomalous dependence of the conductance peak height on T_{max} and/or probing frequency (f_T) not observed by any junction spectroscopy technique employed to ZnO so far. This behavior is consistent with the attribution of D_X to the ++/+ transition of a negative-U like defect of donor-like with an energy barrier for atomic reconfiguration of $\sim 0.2 - 0.3$ eV. On the basis of the comparison of these findings with theoretical results recently published, the D_X peak is attributed to the $V_O^{+/++}$ level and the $\sim 0.2 - 0.3$ eV barrier to the transition from the V_O^{++} to the V_O^{0} state involving a two electron capture process.

5.5 Paper V

In paper V it is found possible to achieve *SC*s by using ordinary organic solvents cleaning when Pd contacts are deposited on high resistivity hydrothermally grown ZnO samples. First, the samples have been annealed at 800 ^oC for 1 h. Then, a low dose H implantation has been used to decrease the material resistivity and form a *n*-type doped layer with a width of ~ 4 μm and a resisitivity as low as ~ 0.4 $\Omega \cdot$cm after a post implantation annealing for 30 min at 200 ^oC in N_2. Finally, af-

ter organic solvents cleaning Pd *SC*s have been deposited. This procedure shows promising results with *SC*s having a rectification ratio, taking ratio between the forward and reverse current at +2 V and - 2 V, of up to $\sim$ 3 orders of magnitude. However, the high degree of compensation and challenge to accurately control the charge carrier concentration below the $\sim 10^{17}$ cm^{-3} range is severely limiting the applicability of this method for these samples.

5.6 Concluding remarks and suggestions for further studies

In conclusion, a procedure to obtain *SC*s with high rectification ratio, a thermal stability up to $\sim 200\ ^{o}$C and relatively high long term stability has been established and the physics behind the effectiveness of this procedure has been investigated. However, all the results presented have been obtained for Pd, while no systematic study of the dependence on the metal used for the *SC*s has been made. The results shown and present in the literature, so far, suggest that some kind of oxidation treatment is beneficial to the formation of *SC*s with high rectification ratios, possibly combined with the choice of a *SC*s metal that forms oxides with high work function. Therefore, on one hand, the investigation of other oxidation agents with higher oxidation power than H_2O_2, like Ozone or Flourine treatments, can lead to interesting results. On the other hand, also keeping the pre-treatments parameters fixed and determine the effects of different contact metals according to their chemical tendency to form oxides should be of great interest.

Furthermore, this thesis has been focused mainly on the O-face $(000\overline{1})$ and only

few (not successful) attempts have been made to realize *SC*s on the Zn face, and the effect of treating the Zn face with H_2O_2 should be studied systematically. All these studies could lead to *SC*s with even better performance and to a better understanding of the process to achieve high quality *SC*s to ZnO. In addition, no detailed investigation of the changes by using H_2O_2 for different oxidation times has been performed. This is mainly due to the intrinsic differences between the as received samples used, which are high enough to mask the results of a more detailed study. Hence, also an optimization of the H_2O_2 pre-treatment has to be performed when the hydrothermal growth process has become controllable enough to produce samples with less scatter in physical properties. Finally, the promising results reported in paper V might be related to the annealings performed prior to the contact deposition and the effect of this pre-treatment deserves further attention.
From a characterization point of view, all the electrical measurements performed indicate a high sensitivity of the material surface on the ambient where the measurements are taken in. That is, changes of the reverse current by at least 1 order of magnitude have been routinely observed by acquiring data with the sample placed in air or in vacuum, and therefore a procedure to increase the ZnO surface passivation, beside using H_2O_2, represents another important goal to achieve.
In addition, more insight into the nature of the point defects is needed. While, there is some consensus in the literature on the assignment of the D_1 level to a Hydrogen related defect, the nature of E_3 (D_3) is still unknown. Due to its deep nature and the high concentration detected in the samples characterized, E_3 is particular detrimental to any possible device application of ZnO, since it can cause substantial changes in the carrier concentration around room temperature. Moreover, the evidence of a negative-U level has been found and also in this case the

nature of the defect has not been established yet. In both cases, performing electrical characterization on series of annealed and implanted/damaged samples to be combined with techniques like photoluminescence, *SIMS* and positron annihilation spectroscopy measurements might be useful in determining their chemical nature and in finding out possible alternatives to limit their concentration in hydrothermally grown ZnO.

Bibliography

[1] C. Jagadish and S. J. Pearton, *Zinc Oxide Bulk, Thin films and Nanostructures*. Elsevier, Oxford, 2006.

[2] B. K. Meyer, H. Alves, D. M. Hofmann, W. Kriegseis, D. Forster, F. Bertram, J. Christen, A. Hoffmann, M. Straßburg, M. Dworzak, U. Haboeck, , and A. V. Rodina *phys. stat. sol. (b)*, vol. 241, p. 231, 2004.

[3] D. C. Reynolds, D. C. Look, B. Jogai, C. W. Litton, G. Cantwell, and W. C. Harsch *Phys. Rev. B*, vol. 60, p. 2340, 1999.

[4] B. Szyszka *Thin Solid Films*, vol. 351, p. 164, 1999.

[5] D. Look *Materials Science and Engineering B*, vol. 80, p. 383, 2001.

[6] J. D. Albrecht, P. P. Ruden, S. Limpijumnong, W. R. L. Lambrecht, and K. F. Brennan *J. Appl. Phys.*, vol. 86, p. 6864, 1999.

[7] T. Makino, Y. Segawa, M. Kawasaki, A. Ohtomo, R. Shiroki, K. Tamura, and T. Yasuda *Appl. Phys. Lett.*, vol. 78, p. 1237, 2001.

[8] M. Vellekoop, C. Visser, and P. M. Sarro *Sens. Actuators A*, vol. 23, p. 1027, 1990.

[9] S. Yamauchi, H. Handa, A. Nagayama, and T. Hariu *thin solid films*, vol. 345, p. 12, 1999.

[10] Please visit the web site http://www.cermetinc.com/.

[11] Please visit the web site http://www.tew.co.jp/e/.

[12] Please visit the web site http://www.spcgoodwill.com/.

[13] M. Suscavage, M. Harris, D. Bliss, P. Yip, S.-Q. Wang, D. Schwall, L. Bouthillette, J. Bailey, M. Callahan, D. C. Look, D. C. Reynolds, R. L. Jones, and C. W. Litton *MRS Internet J. Nitride Semicond. Res.*, vol. 4S1, p. G3.40, 1999.

[14] E. V. Kortunova, N. G. Nikolaeva, P. P. Chvanski, V. V. Maltsev, E. A. Volkova, E. V. Koporulina, N. I. Leonyuk, and T. F. Kuech *J. Mater. Sci.*, vol. 43, p. 2336, 2008.

[15] K. Ip, G. T. Thaler, H. Yang, S. Y. Han, Y. Li, D. P. Norton, S. J. Pearton, S. Jang, and F. Ren *J. Crystal Growth*, vol. 287, p. 149, 2006.

[16] Ü. Özgür, Y. I. Alivov, C. Liu, A. Teke, M. A. Reshchikov, S. Doğan, V. Avrutin, S.-J. Cho, and H. Morkoç *J. Appl. Phys.*, vol. 98, p. 041301, 2005.

[17] P. W. Tasker *J. Phys. C*, vol. 12, p. 4977, 1979.

[18] M. Kunat, S. G. Girol, T. Becker, U. Burghaus, and C. Wöll *Phy. Rev. B*, vol. 66, p. 081402(R), 2002.

[19] B. J. Hopkins and P. A. Taylor *J. Phys. C*, vol. 9, p. 571, 1976.

[20] M. W. Allen, P. Miller, R. J. Reeves, and S. M. Durbin *Appl. Phys. Lett.*, vol. 90, p. 062104, 2007.

[21] X. Yang, C. Xu, and N. C. Giles *Mat. Res. Soc. Symp. Proc.*, vol. 1035, pp. L04–07, 2008.

[22] N. Syrbu, I. M. Tiginyanu, V. V. Zalmai, V. V. Ursaki, and E. V. Rusu *Phys. B.*, vol. 353, p. 111, 2004.

[23] D. L. Rode, *Semiconductors and Semimetals 10.* Academic, London, 1975.

[24] V. F. Petrenko and R. W. Whitworth *Phil .Mag. A.*, vol. 41, p. 681, 1980.

[25] C. Klingshirn, R. Hauschild, J. Fallert, and H. Kalt *Phys. Rev. B*, vol. 75, p. 115203, 2007.

[26] H. Y. Fan *Phys. Rev.*, vol. 82, p. 900, 1951.

[27] F. M. Peeters, P. Warmembol, and J. T. Devreese *Europhys. Lett.*, vol. 3, p. 1219, 1987.

[28] T. Minami, H. Nanto, and S. Takata *Jpn. J.. Appl. Phys.*, vol. 23, p. L280, 1984.

[29] V. Assunção, E. Fortunato, Á. Marques, H. Aguas, I. Ferreira, M. Costa, and R. Martins *Thin solids Films*, vol. 427, p. 401, 2003.

[30] J. M. Phillips, R. J. Cava, G. A. Thomas, S. A. Carter, J. Kwo, T. Siegrist, J. J. Krajewski, J. H. Marshall, W. F. P. Jr., and D. H. Rapkine *Appl. Phys. Lett.*, vol. 67, p. 2246, 1995.

[31] D. C. Look, J. W. Hemsky, and J. R. Sizelove *Phys. Rev. Lett.*, vol. 82, p. 2552, 1999.

[32] A. Janotti and C. G. v. Walle *Nature*, vol. 6, p. 44, 2007.

[33] D. C. Look, G. C. Farlow, P. Reunchan, S. Limpijumnong, S. B. Zhang, and K. Nordlund *Phys. Rev. Lett.*, vol. 95, p. 225502, 2005.

[34] F. D. Auret, S. A. Goodman, M. J. Legodi, W. E. Meyer, and D. C. Look *Appl. Phys. Lett.*, vol. 80, p. 1340, 2002.

[35] H. v. Wenckstern, M. Brandt, H. Schmidt, G. Biehne, R. P. H. Hochmuth, M. Lorenz, and M. Grundmann *Appl. Phys. A*, vol. 88, p. 135, 2007.

[36] F. D. Auret, W. E. Meyer, P. J. J. v. Rensburg, M. Hayes, J. M. Nel, H. v. Wenckstern, H. Hochmuth, G. Biehne, M. Lorenz, and M. Grundmann *J. Phys: Conf. Ser.*, vol. 100, p. 042038, 2008.

[37] J. C. Simpson and J. F. Cordaro *J. Appl. Phys.*, vol. 63, p. 1781, 1987.

[38] Y. Jiang, N. C. Giles, and L. E. Halliburton *J. Appl. Phys.*, vol. 101, p. 093706, 2007.

[39] G. Brauer, W. Anwand, W. Skorupa, J. Kuriplach, O. Melikhova, C. Moisson, H. von Wenckstern, H. Schmidt, M. Lorenz, and M. Grundmann *Phys. Rev. B*, vol. 74, p. 045208, 2006.

[40] A. F. Kohan, G. Ceder, D. Morgan, and C. G. V. Walle *Phys. Rev. B*, vol. 61, p. 15019, 2000.

[41] C. H. Park, S. B. Zhang, and S. Wei1 *Phys. Rev. B*, vol. 66, p. 073202, 2002.

[42] D. C. Look, D. C. Reynolds, C. W. Litton, R. L. Jones, D. B. Eason, and G. Cantwell *Appl. Phys. Lett.*, vol. 81, p. 1830, 2002.

[43] K. Kim, H. Kim, D. Hwang, J. Lim, and S.Park *Appl. Phys. Lett.*, vol. 83, p. 63, 2003.

[44] F. X. Xiu, Z. Yang, L. J. Mandalapu, D. T. Zhao, and J. L. L. andW. P. Beyermann *Appl. Phys. Lett.*, vol. 87, p. 152101, 2005.

[45] D. C. Look, G. M. Renlund, R. H. B. II, and J. R. Sizelove *Appl. Phys. Lett.*, vol. 85, p. 5269, 2004.

[46] L. H. Rhoderick and R. H. Williams, *Metal-Semiconductor Contacts*. Clarendon Press, 1988. cap. 1.

[47] H. v. Wenckstern, Ph.D thesis, Universit¨at Leipzig, Leipzig, Germany, 2007.

[48] S. A. Campbell, *The Science and Engineering of Microelectronic Fabrication*. Oxford University Press, 2001. cap. 15.

[49] S. Kurtin, T. C. McGill, and C. A. Mead *Phys. Rev. Lett.*, vol. 22, p. 1433, 1969.

[50] S. G. Louie, J. R. Chelikowsky, and M. L. Cohen *Phys. Rev. B*, vol. 15, p. 2154, 1977.

[51] C. A. Mead *Phys. Lett.*, vol. 18, p. 218, 1965.

[52] R. H. Williams *Phys. Scr.*, vol. T29, p. 209, 1989.

[53] D. C. Look, B. Claflin, and H. E. Smith *Appl. Phys. Lett.*, vol. 92, p. 122108, 2008.

[54] L. J. Brillson, H. L. Mosbacker, M. J. Hetzer, Y. Strzhemechny, G. H. Jessen, D. C. Look, G. Cantwell, J. Zhang, and J. J. Song *Appl. Phys. Lett.*, vol. 90, p. 102116, 2007.

[55] A. Y. Polyakov, N. B. Smirnov, E. A. Kozhukhova, V. I. Vdovin, K. Ip, Y. W. Heo, D. P. Norton, and S. J. Pearton *Appl. Phys. Lett.*, vol. 83, p. 1575, 2003.

[56] H. L. Mosbacker, Y. M. Strzhemechny, B. D. White, P. E. Smith, D. C. Look, D. C. Reynolds, C. W. Litton, and L. J. Brillson *Appl. Phys. Lett.*, vol. 87, p. 012102, 2005.

[57] B. J. Coppa, R. F. Davis, and R. J. Nemanich *Appl. Phys. Lett.*, vol. 82, p. 400, 2003.

[58] M. W. Allen, P. Miller, R. J. Reeves, and S. M. Durbin *Appl. Phys. Lett.*, vol. 90, p. 062104, 2007.

[59] Y. Dong, Z.-Q. Fang, D. C. Look, G. Cantwell, J. Zhang, J. J. Song, and L. J. Brillson *Appl. Phys. Lett.*, vol. 93, p. 072111, 2008.

[60] H. Sheng, S. Muthukumar, N. W. Emanetoglu, , and Y. Lu *Appl. Phys. Lett.*, vol. 80, p. 2132, 2003.

[61] V. E. Henrich and P. A. Cox, *The Surface Science of Metal Oxides*. Cambridge University Press, 1994. cap. 1, 6.

[62] U. Grossner, S. Gabrielsen, T. M. Børseth, J. Grillenberger, A. Y. Kuznetsov, and B. G. Svensson *Appl. Phys. Lett.*, vol. 85, p. 2259, 2004.

[63] S. Kim, H. Kim, and T. Seong *Appl. Phys. Lett.*, vol. 86, p. 112101, 2004.

[64] Q. L. Gu, C. C. Ling, X. D. Cheng, A. M. C. Ng, C. D. Beling, S. Fung, A. B. Djurišić, L. W. Lu, G. Brauer, and H. C. Ong *Appl. Phys. Lett.*, vol. 122101, p. 90, 2007.

[65] S. Kim, H. Kim, and T. Seong *Appl. Phys. Lett.*, vol. 86, p. 022101, 2005.

[66] H. Endo, M. Sugibuchi, K. Takahashi, S. Goto, and S. Sugimura *Appl. Phys. Lett.*, vol. 90, p. 121906, 2007.

[67] M. W. Allen, S. M. Durbin, and J. B. Metson *Appl. Phys. Lett.*, vol. 91, p. 053512, 2007.

[68] H. von Wenckstern, E. M. Kaidashev, M. Lorenz, H. Hochmuth, G. Biehne, J. Lenzner, V. Gottschalch, R. Pickenhain, and M. Grundmann *Appl. Phys. Lett.*, vol. 84, p. 79, 2004.

[69] M. W. Allen, M. M. Alkaisi, and S. M. Durbin *Appl. Phys. Lett.*, vol. 89, p. 103520, 2006.

[70] D. H. M. Oh, J. Lim, Y. Choi, and S. Park *Appl. Phys. Lett.*, vol. 91, p. 042109, 2007.

[71] S. O. Kucheyev, J. E. Bradby, J. S. Williams, C. Jagadish, and M. V. Swain *Appl. Phys. Lett.*, vol. 80, p. 956, 2002.

[72] Please visit the web site http://www.spmtips.com/howto/mode/cm.

[73] J. H. Werner *Appl. Phys. A*, vol. 47, p. 291, 1998.

[74] B. J. Coppa, C. C. Fulton, S. M. Kiesel, R. F. Davis, C. Pandarinath, J. E. Burnetteì, R. J. Nemanich, and D. J. Smith *J. Appl. Phys.*, vol. 97, p. 103517, 2005.

[75] P. Blood and J. W. Orton, *The Electrical Characterization of Semiconductors: Majority Carriers and Electron States*. Academic, 1992. cap. 1, 6.

[76] J. L. Pautrat, B. Katircioglu, N. Magnea, D. Bensahel, J. C. Pfister, and L. Revoil *Solid-St. Electron.*, vol. 23, p. 1159, 1980.

[77] D. L. Losee *J. Appl. Phys.*, vol. 46, p. 2204, 1975.

[78] G. Vincent, D. Bois, and P. Pinard *J. Appl. Phys.*, vol. 46, p. 5173, 1975.

[79] M. Beguwala and C. R. Crowell *Solid-St. Electron.*, vol. 17, p. 203, 1974.

[80] C. T. Sah and V. G. K. Reddi *IEEE Trans. Electron Devices*, vol. 11, p. 345, 1964.

[81] C. Ghezzi *Appl. Phys. A*, vol. 26, p. 191, 1981.

[82] J. W. Lee, J. D. Cohen, and W. N. Shafarman *Thin Solid Films*, vol. 480-481, p. 336, 2005.

[83] H. von Wenckstern, H. Schmidt, M. Grundmann, M. W. Allen, P. Miller, R. J. Reeves, and S. M. Durbin *Appl. Phys. Lett.*, vol. 91, p. 022913, 2007.

[84] R. Chwang, B. J. Smith, and C. R. Crowell *Solid-St. Electron.*, vol. 17, p. 1217, 1974.

[85] B. Sapoval and C. .Hermann, *Physics of Semiconductor*. Springer-Verlag, 1995.